Terahertz Radiation from Semiconductors

Jie Shan[1] and Tony F. Heinz[2]

[1] Department of Physics, Case Western Reserve University
Cleveland, OH 44106, USA
[2] Departments of Physics and Electrical Engineering, Columbia University
New York, NY 10027, USA
tony.heinz@columbia.edu

Abstract. We provide a review of the different schemes for generating terahertz (THz) radiation using photoconductive emitters excited by femtosecond lasers. The discussion is concerned principally with large-area emitters because of their relative simplicity, both in fabrication and analysis, and their capabilities for high-power THz generation. In addition to discussing the principal characteristics of these emitters, we present a simple, but unified description of their behavior. The principal ingredients in this description are a Drude–Lorentz model for the carrier dynamics combined with a suitable solution of the radiation problem for a current sheet. This formalism permits one to examine the nature of the generated THz waveforms in the near and far field, as well as to consider the effect of the material properties and excitation conditions on the THz emission process. Within this picture, we describe the origin of the strong enhancement in THz emission that is observed upon application of an external magnetic field to emitters relying on transient photocurrents flowing perpendicular to the surface. Saturation processes that limit the efficiency of THz emission are also an important feature of these devices. These effects are discussed in terms of perturbation of the bias field induced by space-charge screening and the THz radiation field.

1 Introduction

The notion of using ultrashort laser pulses to trigger ultrafast electrical pulses dates back to the early development of modelocked lasers. The initial investigations involved the production and measurement of ultrashort electrical pulses guided by transmission lines through the use of a laser-triggered photoconductive switch [1,2,3]. Researchers also recognized that such devices could be used as photoconductive antennas to couple radiation into or collect radiation from free space [4,5]. Many researchers contributed to important refinements of such devices, including optimization of the time response of the photoconductive switches through the use of new materials and geometries and the development of improved antenna structures [1,2,6,7]. The combination of an emitter of electromagnetic radiation triggered by an ultrafast laser pulse and a detector of this radiation gated by a time-synchronized excitation pulse permitted the development of a novel time-domain spectrometer [1,2]. The resulting method of THz time-domain spectroscopy (THz TDS) has provided a powerful new tool for measurements in a range of frequencies from

Kong-Thon Tsen (Ed.): Ultrafast Dynamical Processes in Semiconductors,
Topics Appl. Phys. **92**, 1–59 (2004)

a fraction to several THz ($1\,\mathrm{THz} = 10^{12}\,\mathrm{Hz}$) in the far-infrared. Such time-domain measurements yield, upon Fourier transformation, a complete characterization of the complex transmission/reflection coefficients of a sample as a function of frequency. This in turn permits the determination of complex dielectric function or, equivalently, the complex conductivity, of the sample, a capability that has been successfully applied to a large variety of material systems [2,8,9,10,11,12,13,14,15,16,17,18,19,20,21,22,23,24,25,26,27,28].

A further noteworthy development of THz techniques based on ultrafast lasers was the demonstration of large-area photoconductive emitters in the early 1990s [29,30,31]. These devices also rely on the motion of photoinduced charge carriers in the presence of an electrical bias field, but are constructed so that a large region of the photoconductor is illuminated. They are not appropriate for producing ultrafast electric-field transients on transmission lines. Rather, they are optimized for radiating THz pulses directly into free space. For this purpose they offer some potential advantages with respect to emitters based on small photoconductive gaps and metallic antenna structures. Principal among these is the possibility of scaling the device to produce high-power THz emission [32]. This feature is a direct consequence of the possibility of expanding the lateral area of the irradiated region and thus avoiding saturation effects that are present in any photoconductive device at sufficiently high laser fluence. In addition, from the practical standpoint, the structures are very simple to fabricate. With respect to the radiation properties, the large emission area implies the possibility of generating a relatively collimated beam of THz radiation, a desirable property for many applications. In fact the direction of this emission may be controlled by the angle of incidence of the laser pump beam [30,33]. Finally, the lack of antenna structures implies that the spectral characteristics of the THz emission will be limited only by the inherent carrier dynamics and the properties of the pump laser, which enables a broad spectral response [34].

Such large-area photoconductive emitters may be classified according to the direction of flow of the transient photocurrent. One scheme involves the application of an electrical bias field in the plane of the surface by means of a pair of widely separated electrodes. These devices are the so-called large-aperture emitters and they produce photocurrent transients directed along the surface. The other class of devices has a bias field perpendicular to the surface. The relevant bias field may be produced by intrinsic band bending associated with trapped charges at the surface in a depletion field device or may be externally applied in a p–i–n or Schottky-barrier structure. Although the details of the behavior of the photocurrent differ depending on the geometry of the problem, these large-area photoconductive emitters share many common properties and can be discussed within the same general framework of carrier transport and radiation properties.

In this chapter, we restrict our discussion of photoconductive THz emitters to the behavior of such large-area emitters. Some of their attractive

features as sources of THz radiation have been indicated above. From the point of view of this chapter, which emphasizes the fundamental aspects of THz emission and its relation to basic concepts in radiation theory and carrier dynamics, they are also appealing because of their simplicity. These devices can be considered essentially as a photocurrent radiating into free space. Their analysis does not require consideration of antenna response nor of semiconductor/electrode interfaces. Furthermore, these emitters have been the subject of many investigations. The nature of the THz emission has been characterized in the spectral and temporal domains. Studies have also examined the dependence of the THz radiation on important parameters in the problem, such as the excitation geometry, the laser-pulse duration and fluence, the magnitude and direction of the bias field, and the properties of the photoconductive medium. The saturation properties of large-area emitters at high laser fluence, an important parameter for overall efficiency, have also been investigated both experimentally and theoretically. An additional aspect that has attracted significant interest is the influence of applied magnetic fields on the THz emission. Especially for the case of depletion-field devices, external magnetic fields were found to have a dramatic impact on the radiation efficiency. With this wealth of interesting phenomena and knowledge at hand, we attempt to provide a review of the basic features of large-area emitters. Particular emphasis will be given to the influence of magnetic fields and saturation effects, two active areas of recent research.

The organization of this chapter is as follows. In Sect. 2, we present the basic results for radiation from a current sheet located near the interface of two dielectric media. In view of the relatively long wavelength of the THz emission, this model is sufficient to describe the behavior of all of the large-area THz emitters. Section 3 is devoted to a presentation of a description of carrier dynamics, both from the standpoint of a general response function and as embodied in the Drude–Lorentz model. The latter, while certainly not sufficient to describe many subtle aspects of THz emission, provides a concrete and specific framework for the discussion of the different types of emitters, the relation of the emission to material properties, the nature of saturation effects, and the influence of external magnetic fields. With the basic ingredients presented in Sects. 2 and 3 for the radiation problem and carrier dynamics, we then turn in Sect. 4 to an overview of the basic characteristics of large-area THz emitters that have been observed experimentally. Section 5 considers a series of experiments related to the influence of externally applied magnetic fields. The large enhancement in THz emission observed from emitters with current flow normal to the surface can be understood by combining the Drude–Lorentz model of carrier dynamics with a suitable analysis of the radiation properties of such current transients. The topic of transient modification of the bias field induced during the THz emission process is considered in Sect. 6. This issue is both of fundamental interest and of direct significance in understanding the saturation effects that limit the emission efficiency of

such devices. A few concluding remarks are offered in Sect. 7, the last of this chapter.

2 THz Radiation from Transient Currents in Large-Area Emitters

In this section, we review the basic laws governing the radiation process relevant for the production of THz emission from a large-area photoconductive source following excitation by an ultrafast laser pulse. We present expressions for the radiated electric field in the near- and far-field zones in terms of the transient photocurrent. We describe the polarization properties and angular dependence of the emission under different conditions, and examine factors determining the radiation efficiency. We reserve for the next section a discussion of the nature of the transient photocurrent and its relation to basic material properties. Here we consider the current to be a given quantity and examine the consequences for THz emission.

2.1 Overall Configuration and Nonlinear Snell's Law

The situation of interest is depicted schematically in Fig. 1. An ultrashort laser pulse is incident on the surface of a photoconductor at an angle of incidence θ. The ultrashort laser pulse generates photocarriers, which then move under the influence of an electrical bias field. The bias field may be either externally applied (parallel or perpendicular to the surface) or internally generated by band bending from trapped surface charges (perpendicular to the surface). The resulting transient photocurrent gives rise to the emission of THz electromagnetic pulses in the reflected and transmitted directions.

For the case of a large-area device, we are concerned with an incident laser beam that has spatial dimensions several times that of the THz wavelength being generated. A well-collimated incident optical beam will then produce collimated beams of THz radiation. These beams will be emitted in the reflected and transmitted directions defined by the generalized Snell's law:

$$n_1(\omega)\sin\theta = n_1(\Omega)\sin\theta_1^{\Omega} = n_2(\Omega)\sin\theta_2^{\Omega}\,. \tag{1}$$

Here ω and Ω denote, respectively, the optical and THz frequencies; 1 refers to the medium through which the laser beam is incident and 2 to the photoconductive medium; n_i (ω or Ω) denotes the refractive index (assumed to be isotropic) in the appropriate medium evaluated at the relevant frequency. This expression can be understood most readily by considering the process of photoconductivity in a biased sample as a manifestation of a second-order nonlinear optical mixing process. In this view, the THz radiation is formed by difference-frequency mixing of the Fourier components contained within

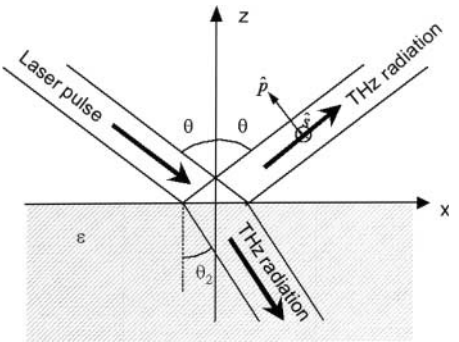

Fig. 1. Scheme for the generation of THz radiation from a large-area photoconductive emitter. An ultrashort excitation pulse is incident on the photoconductive medium at an angle θ. The induced photocurrent gives rise to reflected and transmitted beams of THz radiation. The THz dielectric constant of the photoconductor is ε. The induced photocurrent is confined to a thin region below the surface and is treated as a current sheet

the optical pump pulse. The well-known nonlinear Snell's law then corresponds simply to a statement of conservation of the in-plane component of the wavevector. If we regard the generation process in the time domain, we may identify the specified reflected and transmitted directions as those for which emission from different spatial elements of the surface current sheet radiates in phase. Thus, a sharp peak in the emission appears in these particular directions. For the purposes of the discussion in this chapter, we will be concerned with the usual case where the photoconductor is illuminated in air. We then see that the reflected THz beam will emerge at an angle $\theta_1 = \theta$, just as for the usual linear reflection (under the well-justified neglect of the slight dispersion in air). For convenience, we also introduce the dielectric function of the photoconductor at THz frequencies ε. In terms of this quantity, the transmitted wave will travel at an angle θ_2 defined by $\sqrt{\varepsilon}\sin\theta_2 = \sin\theta$, where we again neglect the dispersion of the material response over the relevant range of THz frequencies.

Before considering the solution for the strengths of these radiated fields, we introduce one additional assumption: that photocurrent is confined to a sheet that is thin compared to the THz wavelength. Given typical penetration depths for the laser radiation in a photoconductive medium of less than 1 μm, this criterion is generally very well satisfied in practice. Under these circumstances, the radiation process is defined entirely by the surface current density $\boldsymbol{J}_\mathrm{s}$, i.e., by the volume current density integrated over the coordinate perpendicular to the surface. As we shall discuss below, for such a current sheet, the radiation field (in the near-field zone) can be found directly by the application of a suitable set of boundary conditions. An explicit expression for the far-field solution for the THz emission can then be obtained by propagation of the near-field solution within the Fraunhofer approximation.

2.2 Boundary Conditions for Surface Photocurrent

The relevant boundary conditions for a current sheet can be adapted directly from the discussion of a polarization sheet previously developed in the context of surface second-harmonic generation [35]. These boundary-matching conditions follow from Maxwell's equations with a transient source polarization $\boldsymbol{P}(t)$. In CGS units they read as

$$\begin{aligned} \boldsymbol{\nabla} \cdot \boldsymbol{D} &= -4\pi \boldsymbol{\nabla} \cdot \boldsymbol{P}\,, \\ c\boldsymbol{\nabla} \times \boldsymbol{E} + \frac{\partial \boldsymbol{B}}{\partial t} &= 0\,, \\ \boldsymbol{\nabla} \cdot \boldsymbol{B} &= 0\,, \\ c\boldsymbol{\nabla} \times \boldsymbol{H} - \frac{\partial \boldsymbol{D}}{\partial t} &= 4\pi \frac{\partial \boldsymbol{P}}{\partial t}\,. \end{aligned} \tag{2}$$

Here the transient $\boldsymbol{D}$ and $\boldsymbol{H}$ fields are related to the transient $\boldsymbol{E}$ and $\boldsymbol{B}$ fields by the usual relations for linear response, $\boldsymbol{D} = \overleftrightarrow{\boldsymbol{\varepsilon}}\boldsymbol{E}$ and $\boldsymbol{H} = \overleftrightarrow{\boldsymbol{\mu}}^{-1}\boldsymbol{B}$ and do not include any contribution from the transient source term. In the discussion below, we neglect magnetic response, and take $\boldsymbol{H} = \boldsymbol{B}$.

Using the traditional approach of integrating Maxwell's equations over suitable surfaces and volumes crossing the interface and carefully taking the limit as the thickness of the interfacial region goes to zero, we can derive the matching conditions across the interface. We denote the in-plane directions as x and y, and the normal coordinate as z. The electric and magnetic fields on either side of a polarization sheet $\boldsymbol{P}_{\mathrm{s}}(x, y, t)$ [with a volume polarization $\boldsymbol{P}_{\mathrm{s}}(x, y, t)\delta(z)$] are found to satisfy the following boundary conditions [35]:

$$\begin{aligned} \Delta\, D_z &= -4\pi \boldsymbol{\nabla}_{||} \boldsymbol{P}_{\mathrm{s}}\,, \\ \Delta\, \boldsymbol{E}_{||} &= (-4\pi/\varepsilon)\boldsymbol{\nabla}_{||} P_{\mathrm{s},z}\,, \\ \Delta\, B_z &= 0\,, \\ \Delta\, \boldsymbol{H}_{||} &= (4\pi/c)(\partial \boldsymbol{P}_{\mathrm{s}}/\partial t \times \hat{\boldsymbol{z}})\,. \end{aligned} \tag{3}$$

Here the subscript $||$ refers to components parallel to the surface and $\boldsymbol{\nabla}_{||} \equiv \hat{\boldsymbol{x}}(\partial/\partial x) + \hat{\boldsymbol{y}}(\partial/\partial y)$. In order to convert these relations to the language of a surface current density, we simply apply the identity of $\boldsymbol{J}_{\mathrm{s}}(x, y, t) = \partial \boldsymbol{P}_{\mathrm{s}}(x, y, t)/\partial t$.

From these boundary conditions, one can determine general expressions for the radiation fields in a straightforward fashion.

2.3 THz Radiation Excited at Normal Incidence

In large-aperture photoconductive emitters with an in-plane bias field, current flows only along the surface. Such devices are typically excited by ultrafast laser pulses at normal incidence. In this case, every spatial element of the

emitter is in phase, and the radiated field is independent of the orientation of the bias field with respect to the incident laser beam. For concreteness, we take the surface current sheet to be flowing in the y-direction, with $\boldsymbol{J}_\mathrm{s} = J_\mathrm{s}\hat{\boldsymbol{y}}$.

In this geometry, the wavevectors are along the surface normal. The radiated electric and magnetic fields thus have only components parallel to the surface. The boundary conditions of (2) and (3) can be simplified to give

$$\begin{aligned} E_1 - E_2 &= 0\,, \\ H_1 - H_2 &= (4\pi/c)\boldsymbol{J}_\mathrm{s} \times \hat{\boldsymbol{z}}\,. \end{aligned} \tag{4}$$

In addition, for a large-area emitter where the pump radiation can be treated as a plane wave, the radiated THz emission can also be approximated by a plane wave. In this case, the magnetic-field and electric field components are related in the usual way as

$$\begin{aligned} H_1 \times \hat{z} &= E_1\,, \\ H_2 \times \hat{z} &= -\sqrt{\varepsilon}E_2\,. \end{aligned} \tag{5}$$

Combining (4) and (5), we then obtain directly the resultant THz radiation fields of

$$\boldsymbol{E}_1 = \boldsymbol{E}_2 = -\frac{4\pi}{c}\frac{1}{1+\sqrt{\varepsilon}}\boldsymbol{J}_\mathrm{s} = -\frac{4\pi}{c}\frac{1}{1+\sqrt{\varepsilon}}J_\mathrm{s}\hat{\boldsymbol{y}} \tag{6}$$

in the near-field zone.

In order to obtain the THz radiation in the far-field zone (where diffraction of the THz beam has become extensive), we apply field propagation in the Fraunhofer approximation. This yields for the peak electric field (along the center of the direction of propagation), the expression

$$\boldsymbol{E}_1(t) \cong -\frac{2A}{c^2 r}\frac{1}{1+\sqrt{\varepsilon}}\frac{\partial J_\mathrm{s}}{\partial t}\hat{\boldsymbol{y}}\,. \tag{7}$$

Here A denotes the area of the surface layer in which the current density, $\boldsymbol{J}_\mathrm{s}(t)$, is present; r is the distance of propagation; and the quantity $\partial J_\mathrm{s}(t)/\partial t$ is evaluated at the retarded time $t' = t - r/c$.

2.4 THz Radiation Excited at Oblique Incidence

We now consider the more general case of THz radiation generated by an ultrafast laser pulse incident on the photoconductor at an oblique angle θ. This excitation geometry, as we show below, is necessary for large-area emitters based on bias fields that are perpendicular to the surface. All four boundary conditions of (3) are required to specify the radiated fields. The solution is, however, well known and we simply quote the result [36]. For this case, in addition to the $\hat{s} = \hat{y}$ polarized radiation, we also obtain the $\hat{p} = -\cos\theta\hat{x} + \sin\theta\hat{z}$

polarized radiation. The radiated electric fields reflected from the surface of the emitter are given in the near field by:

$$E_{\mathrm{s}}(t) = -\frac{4\pi}{c}\frac{1}{\cos\theta + \sqrt{\varepsilon - \sin^2\theta}}(\boldsymbol{J}_{\mathrm{s}} \cdot \hat{\boldsymbol{y}})$$
$$E_{\mathrm{p}}(t) = -\frac{4\pi}{c}\frac{\sin\theta}{\varepsilon\cos\theta + \sqrt{\varepsilon - \sin^2\theta}}\left(\boldsymbol{J}_{\mathrm{s}} \cdot \hat{\boldsymbol{z}} - \gamma \boldsymbol{J}_{\mathrm{s}} \cdot \hat{\boldsymbol{x}}\right), \tag{8}$$

where the dimensionless parameter $\gamma \equiv \sqrt{\varepsilon - \sin^2\theta}/\sin\theta$.

The corresponding relations for the far field can again be obtained within the Fraunhofer approximation as

$$E_{\mathrm{s}}(t) = -\frac{2A}{c^2 r}\frac{1}{\cos\theta + \sqrt{\varepsilon - \sin^2\theta}}\left(\frac{\partial \boldsymbol{J}_{\mathrm{s}}}{\partial t} \cdot \hat{\boldsymbol{y}}\right),$$
$$E_{\mathrm{p}}(t) = -\frac{2A}{c^2 r}\frac{\sin\theta}{\varepsilon\cos\theta + \sqrt{\varepsilon - \sin^2\theta}}\left(\frac{\partial \boldsymbol{J}_{\mathrm{s}}}{\partial t} \cdot \hat{\boldsymbol{z}} - \gamma\frac{\partial \boldsymbol{J}_{\mathrm{s}}}{\partial t} \cdot \hat{\boldsymbol{x}}\right). \tag{9}$$

We see from these expressions that in the near-field zone, the time evolution of the THz electric field follows (an appropriately weighted projection of) the surface current density $\boldsymbol{J}_{\mathrm{s}}$. In the far-field zone, the THz electric field does the same for time derivatives of the surface current density, $\partial \boldsymbol{J}_{\mathrm{s}}/\partial t$. In a simple physical picture of constant carrier density of the photocurrent, in the near field, we see that $E(t)$ is related to the velocity of the charge carriers, while in the far field, $E(t)$ is related to the acceleration of these carriers.

2.5 Geometrical Factors in THz Radiation Efficiency

As just noted the *waveform* of the (near-field) radiated THz electric field is determined by the temporal evolution of the transient photocurrent. It has no particular relation to the geometrical configuration of the sample or of the laser excitation. The *amplitude* of the THz emission is, however, strongly dependent on these parameters. This effect is illustrated in Fig. 2. In this example, we have set $\varepsilon = 13.1$, corresponding to the case of a GaAs photoconductor. The figures show the relative amplitudes of the *s*- and *p*-polarized components of the THz radiation induced by a current transient flowing in the *x*-, *y*-, or *z*-direction. The dependence of these quantities is plotted as a function of the angle of incidence, which equals the emission angle for the reflected THz radiation. No consideration has been given to changes in the reflectivity of the pump beam, so these results correspond simply to the radiation effects. A few remarks with reference to the figure should be made here. First, at normal incidence ($\theta = 0$), there is no coupling to currents flowing normal to the surface. Thus, simple THz emitters based on perpendicular bias fields cannot operate at normal incidence. Secondly, at an oblique incident angle, the figures show that for a current confined to the plane of the surface, the component lying in the plane of incidence (J_x) is

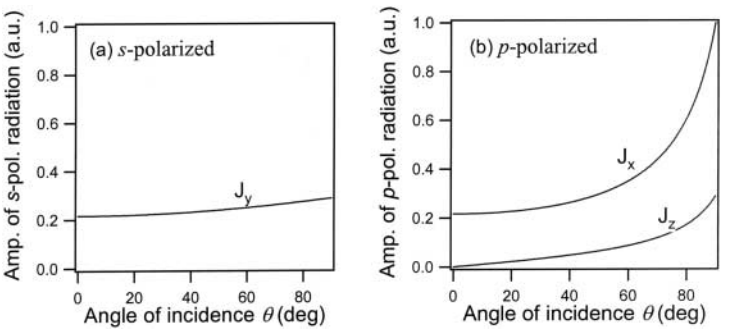

Fig. 2. Calculated relative efficiency of (**a**) *s*- and (**b**) *p*-polarized reflected THz electric fields generated by transient photocurrents flowing in differing directions as a function of the angle of incidence θ. The sample is characterized by $\varepsilon = 13.1$, corresponding to GaAs. Reflection losses of the pump laser beam are not included, so the results represent only the relative radiation efficiency

a more efficient radiation source than the current perpendicular to the plane of incidence (J_y). This effect arises from the differing boundary conditions for *s*- and *p*-polarized radiation.

Finally, an observation that will be critical in explaining the magnetic-field-induced enhancement of THz emission (discussed in Sect. 5) concerns the relative radiation efficiency of the tangential (J_x) and perpendicular (J_z) components of the photocurrent that contribute to *p*-polarized emission. As Fig. 2 illustrates, the former can be many times greater than the latter. More precisely, we see from (8) or (9) that J_x actually radiates γ times more efficiently than J_z. For materials, such as the photoconductors of interest with $\varepsilon \gg 1$, the factor $\gamma = \sqrt{\varepsilon - \sin^2\theta}/\sin\theta$ will be large. In particular, as the angle θ decreases, the radiation efficiency for J_z goes to zero and γ actually approaches infinity. The physical origin of this effect is clear. Because of the large dielectric constant in photoconductive materials, the THz wavevector inside the material is oriented close to the surface normal for all angles of incidence. However, only the transverse component of the current can radiate. This strongly favors coupling to currents flowing along the plane of the surface compared to those flowing perpendicular to it.

3 Models of the Transient Photocurrent

In the previous section we provided a description of the electromagnetic radiation from a large-area photoconductor. To complete the picture of THz emission, we need to complement this element with a description of the origin of the transient current density and how this quantity is related to the nature of the laser excitation, the bias field, and the properties of the photoconductive medium. In this section, we first consider a purely phenomenological

description of the material in terms of appropriate response functions. Subsequently, we present the simple, but useful description of the carrier response embodied in the Drude–Lorentz model.

3.1 Current Density in Terms of Response Functions

One method of introducing the material response is through a conductivity tensor. For a material with a linear response to the driving electric field and time-invariant properties, this relation is particularly simple in the frequency domain where the Fourier transforms of the current density $\boldsymbol{j}(\omega)$ and the driving electric field $\boldsymbol{E}_{\mathrm{b}}(\omega)$ are related by the conductivity tensor $\overleftrightarrow{\boldsymbol{\sigma}}(\omega)$ as

$$\boldsymbol{j}(\omega) = \overleftrightarrow{\boldsymbol{\sigma}}(\omega)\boldsymbol{E}_{\mathrm{b}}(\omega)\,. \tag{10}$$

In the time domain, the equivalent expression is

$$\boldsymbol{j}(t) = \int_{-\infty}^{t} \overleftrightarrow{\boldsymbol{\sigma}}(t-t')\boldsymbol{E}_{\mathrm{b}}(t')\mathrm{d}t'\,, \tag{11}$$

where the time-domain response, $\overleftrightarrow{\boldsymbol{\sigma}}(t) = 1/2\pi \int_{-\infty}^{\infty} \overleftrightarrow{\boldsymbol{\sigma}}(\omega)\mathrm{e}^{-\mathrm{i}\omega t}\mathrm{d}\omega$, is the inverse Fourier transform of the frequency-domain conductivity $\overleftrightarrow{\boldsymbol{\sigma}}(\omega)$.

The tensorial properties of $\overleftrightarrow{\boldsymbol{\sigma}}$ are frequently unimportant. In media with cubic symmetry, as is normally the case for the semiconductors used for THz emitters, $\overleftrightarrow{\boldsymbol{\sigma}}$ becomes isotropic. We have introduced the tensorial notation, however, because of its relevance for transport in the presence of an external magnetic field, as considered below.

This formulation of the material response in terms of a conductivity tensor has the advantage of permitting one to incorporate the finite carrier response time that is clearly relevant for the subpicosecond transient currents involved in the production of THz radiation. Furthermore, the formulation can readily incorporate time-varying effective bias fields, a situation that results when one considers screening of the static bias field by the carrier response (Sect. 6). It should be stressed, however, that the description as given is still incomplete. It must be modified to account for the critical time-dependent change in the material properties induced by the pump excitation. We consider this aspect in the following discussion.

We also should note before continuing that we have adopted for simplicity of notation a description in terms of a bulk conductivity that relates the driving electric field to the bulk current density. The entire formulation can, however, be recast by introducing a surface conductivity that relates the driving electric field to a surface current density. The latter description is generally appropriate for describing THz emission, for the reasons discussed in Sect. 2 above.

3.1.1 Instantaneous Carrier Response

One limit that is particularly easy to treat is that of an instantaneous material response. In this case, $\overleftrightarrow{\boldsymbol{\sigma}}(\omega)$ is treated as being independent of frequency. The time-domain response can then be written as

$$\overleftrightarrow{\boldsymbol{\sigma}}(t) = \overleftrightarrow{\boldsymbol{\sigma}}_{\mathrm{dc}}\delta(t)\,, \tag{12}$$

where $\overleftrightarrow{\boldsymbol{\sigma}}_{\mathrm{dc}} = \overleftrightarrow{\boldsymbol{\sigma}}(\omega = 0)$ is the usual dc conductivity of the material. In this limit, it is easy to introduce the effect of the changing material properties induced by the pump laser. We do this through the inclusion of a parametric time dependence for $\overleftrightarrow{\boldsymbol{\sigma}}_{\mathrm{dc}}$ to account for changes in the carrier density with time. If the response is dominated by the motion of electrons of charge e, we write

$$\overleftrightarrow{\boldsymbol{\sigma}}_{\mathrm{dc}} = e\overleftrightarrow{\boldsymbol{\mu}}_{\mathrm{dc}}N(t)\,, \tag{13}$$

where $\overleftrightarrow{\boldsymbol{\mu}}_{\mathrm{dc}}$ is the dc mobility of the electrons and $N(t)$ is the time-varying carrier density. This relation could be modified to incorporate a parametric time dependence for the mobility itself, if desired. Such a modification would permit, for example, a description of density-dependent changes in the carrier-scattering rate. The expression could, of course, also be modified to include a contribution from hole transport. The electron contribution generally is considerably larger than that of the holes because of the much higher electron mobility. In view of this fact, and out of a desire to retain simplicity in the expressions, we do not explicitly include the hole contribution to the transient currents in our discussion here and below.

In the limit of instantaneous response of carriers, the time dependence of the current density can then be expressed as

$$\boldsymbol{j}(t) = e\overleftrightarrow{\boldsymbol{\mu}}_{\mathrm{dc}}N(t)\boldsymbol{E}_{\mathrm{b}}(t)\,. \tag{14}$$

This approximation has been widely used in the treatment of saturation effects in large-aperture photoconductive emitters, as discussed in Sect. 6. Strictly speaking, it is valid only when the characteristic time constant of the material response is much shorter than both the time scale over which the driving electric field and the carrier density change significantly. This criterion will apply only for relatively long laser excitation pulses or for very high carrier-scattering rates. Still, it is a very useful relation because of the simplicity it imparts by making the current and bias field exhibit a local relation in time.

3.1.2 Instantaneous Photoexcitation

In general, an accurate description of THz emission from photoconductors requires that the finite response time of the photocarriers in building up

a current be taken into account. In this subsection, we consider the simplified case of instantaneous photocarrier generation. This situation corresponds to excitation by an optical pulse much shorter than the carrier response time and carrier lifetime.

We can model the photocurrent density at time t resulting from carrier injection at time t_0 as the product of the carrier density still persisting at the later time t multiplied by the drift velocity of the carriers at that time. Thus we write for the contribution to the current density at time t from carriers generated in a unit time interval at time t_0

$$\boldsymbol{j}(t, t_0) = eN(t, t_0)\boldsymbol{v}_{t_0}(t)\,. \tag{15}$$

Here the (partial) carrier density at time t from generation at time t_0, denoted by $N(t, t_0)$, is given by the initial contribution multiplied by a function $R_\mathrm{c}(t - t_0)$, as introduced by *Grischkowsky* [2], describing the decay of the number of photogenerated carriers with time. Introducing a factor A to account for the conversion from incident laser intensity to the rate of electron–hole-pair generation in the photoconductor, we can express the carrier density as

$$N(t, t_0) = AR_\mathrm{c}(t - t_0)I_0\,, \tag{16}$$

where I_0 is the laser irradiance.

The carrier drift velocity (in the linear-response regime) can be described by a frequency-domain mobility as $\boldsymbol{v}(\omega) = \vec{\vec{\boldsymbol{\mu}}}(\omega)\boldsymbol{E}_\mathrm{b}(\omega)$. The corresponding expression in the time domain can be stated in terms of the time-domain mobility response function as

$$\boldsymbol{v}_{t_0}(t) = \int_{t_0}^{t} \boldsymbol{\mu}(t - t')\boldsymbol{E}_\mathrm{b}(t')\mathrm{d}t'\,, \tag{17}$$

with the initial condition given at time t_0 of $\boldsymbol{v}(t = t_0) = 0$. Thus, the (partial) photocurrent density resulting from the instantaneous injection of carriers at time t_0 becomes

$$\boldsymbol{j}(t, t_0) = eN(t, t_0)\int_{t_0}^{t} \boldsymbol{\mu}(t - t')\boldsymbol{E}_\mathrm{b}(t')\mathrm{d}t'\,. \tag{18}$$

3.1.3 Excitation by an Arbitrary Laser Pulse

We now generalize the result for the current density produced by an instantaneous pulse of laser radiation to describe a laser pulse with an arbitrary intensity profile $I(t)$. For this case, the current density will involve contributions from carriers present at time t, but generated at all prior times t_0

ranging from $-\infty$ to up to the current time t. Mathematically, we express this as $\boldsymbol{j}(t) = \int_{-\infty}^{t} \boldsymbol{j}(t, t_0)\mathrm{d}t_0$. The (partial) carrier density injected at time t_0 and still persisting at the time t is given by the generalized form of (16) as $N(t, t_0) = AR_\mathrm{c}(t - t_0)I(t_0)$. Thus, the total current density produced by a laser pulse of an intensity profile $I(t)$ can be written as

$$\boldsymbol{j}(t) = eA \int_{-\infty}^{t} \mathrm{d}t_0 I(t_0) R_\mathrm{c}(t - t_0) \int_{t_0}^{t} \boldsymbol{\mu}(t - t')\boldsymbol{E}_\mathrm{b}(t')\mathrm{d}t' \,. \tag{19}$$

To further simplify this expression, we introduce a definite form for the carrier-decay function of $R_\mathrm{c}(t - t_0) = \theta(t - t_0)\mathrm{e}^{-(t-t_0)/\tau_\mathrm{c}}$, corresponding to exponential decay of the density of mobile carriers of a lifetime τ_c. One may then show that (19) can be written (after appropriate partial integration) as

$$\boldsymbol{j}(t) = e \int_{-\infty}^{t} N(t')\mathrm{e}^{-(t-t')/\tau_\mathrm{c}} \vec{\boldsymbol{\mu}}(t - t')\boldsymbol{E}_\mathrm{b}(t')\mathrm{d}t' \,. \tag{20}$$

Here $N(t) = A \int_{-\infty}^{t} R_\mathrm{c}(t - t')I(t')\mathrm{d}t'$ is the total carrier density in the system at any time t.

In the limit of carrier lifetimes longer than the characteristic response time of the mobility function (typically a fraction of a picosecond), we can neglect the exponential decay term in this relation. This expression is then equivalent to a widely used relation in the literature for the transient current [2], but generalized to allow for a time-dependent driving electric field $\boldsymbol{E}_\mathrm{b}(t)$.

3.2 Drude–Lorentz Model

So far we have described the carrier dynamics and transport in terms of conductivity and carrier-mobility functions. The knowledge of these quantities together with a description of the radiation process will unambiguously determine the generation of the THz radiation. Here we introduce a description for the material response based on the Drude–Lorentz model. Before doing so, we briefly examine the temporal evolution of the carriers in terms of the underlying physical processes in semiconductors.

3.2.1 Some Remarks on Carrier Dynamics in Semiconductors Relevant for THz Emission

The ultrafast dynamics of carriers in semiconductors is a complex and widely studied topic. For our discussion, we need to consider the behavior of charge carriers during the short period immediately after photoexcitation when they contribute to the transient current leading to THz emission. The critical

aspects of the problem are thus the process of carrier thermalization, the acceleration of the carriers in the presence of the electric bias field, and the possible loss of carriers through trapping or recombination.

With respect to the thermalization process, this effect arises because photoexcitation generally produces carriers with appreciable excess energy above the bandgap. These so-called hot carriers will equilibrate through carrier–carrier scattering and interactions with the lattice. The duration of the nonthermalized phase depends strongly on the material system, the amount of excess energy of the carriers, and the carrier concentration, but typically falls in the subpicosecond range. From the point of view of THz emission, the relevance of hot carriers lies in the fact that their transport properties may differ significantly from those of thermalized carriers. This effect has been considered in various analyses of THz radiation, for example in *Taylor* et al. [37]. Conversely, the difference in transport properties has been exploited to examine carrier dynamics through analysis of the THz emission properties of photoexcited semiconductors, as exemplified by the recent work of *Hu* et al. [38].

The acceleration of the carriers in the electric bias field is in fact the most critical aspect of the problem for THz emission. This is the process that determines the temporal evolution of the initial photocurrent transient. It can be viewed as involving an initial ballistic acceleration of the carriers on a time scale shorter than the carrier scattering time, followed by an approach to the drift velocity. At low carrier densities in crystalline materials, momentum-changing collisions are usually dominated by phonon-scattering processes. At room temperature, the scattering times typically do not exceed a few tenths of a picosecond. Carrier–carrier scattering may also be important at high carrier densities. For an excitation density of 10^{16}–$10^{18}\,\mathrm{cm}^{-3}$, the scattering time is typically on the order of 10–100 fs. The electron–hole scattering is particularly important when considering transport phenomena, since these collisions can change the momentum in the electron or hole subsystem. Electron–electron scattering, although it does not contribute to the current relaxation due to momentum conservation, plays an important role in establishing thermal equilibrium among electrons. Regardless of its physical origin, the carrier-scattering rate is the key parameter in the description of transport. Carrier acceleration subsequent to photogeneration of an ensemble of charge carriers will persist for a time on the order of the scattering time as the steady-state carrier drift velocity is reached. This behavior is captured in the time-dependent mobility function of the carriers of (17).

On a somewhat longer time scale, one needs to consider processes that lead to the reduction in the density of mobile charge carriers. For pure III–IV materials, radiative recombination of electron–hole pairs would be the dominant mechanism, but would typically take place on the nanosecond time scale. More rapid relaxation can occur through the presence of deep traps or through surface-recombination processes. The reduction of the mobile carrier density is a significant factor for THz generation by ultrashort laser pulses

only when its time scale becomes as short as a few picoseconds. This will generally not be the case for high-purity crystals. It is, however, important in radiation-damaged materials and low-temperature-grown III–V semiconductors in which a deliberate effort is made to reduce the carrier lifetimes. Such materials are widely used in THz systems involving photoconductors integrated into transmission-line structures, applications for which it is often crucial to have a photocurrent transient with a rapid decay. For large-area THz emitters, undamaged materials are usually satisfactory, particularly in the far-field radiation zone where the response is related to the derivative of the photocurrent, rather than to the current itself.

These brief remarks have omitted a description of many of the varied phenomena that can occur. In particular, we would like to remark on the possibility of a more complex response of the carriers in engineered semiconductor nanostructures. In particular, coupled quantum wells can be designed to allow coherent charge oscillations to occur at THz frequencies [39,40,41], thus exploiting another degree of freedom available for THz emitters.

3.2.2 Drude–Lorentz Model for Carrier Transport

Here we present a description of carrier transport within the Drude–Lorentz model. Despite its simplicity, it has been successfully applied to account for the observed behavior of THz emission under several circumstances. *Grischkowsky* used the Drude–Lorentz picture to describe the main features of the observed THz spectra from a photoconductive dipole emitter [2]. Similarly, *Jepsen* and *Keiding* addressed saturation effects using this model [42]. More recently, *Shan* et al. [36] as discussed below in Sect. 5, were able to apply the model to give a semiquantitative explanation of the enhancement of the THz radiation from depletion-field emitters induced by the presence of an external magnetic field.

The Drude–Lorentz model can be obtained from a semiclassical Boltzmann transport description under the assumption of rapid thermalization among the carriers (on a time scale faster than the duration of the laser excitation pulse, τ_{opt}) and negligible carrier diffusion. These conditions are often at least approximately fulfilled. The limitations of the model must, however, be borne in mind. They will be relevant, for example, when the typical scattering length exceeds the physical dimension over which material properties change significantly. This situation can arise in the context of depletion fields or from intentionally structured systems, such as p–i–n diodes. Also, at low temperatures where scattering rates drop, the validity of the Drude–Lorentz model needs to be carefully considered. In many circumstances, beyond its strict range of application, the Drude–Lorentz model will still give a passable description of the carrier dynamics, but may require the use of parameters (effective mass and, particularly, scattering rate) that differ from those of equilibrium carriers.

In the Drude–Lorentz model, the motion of charge carriers under the influence of an external electric bias field $\boldsymbol{E}_{\mathrm{b}}$ and an external magnetic bias field $\boldsymbol{B}$ is assumed to be governed by the following nonrelativistic equation of motion of

$$\frac{\mathrm{d}\boldsymbol{v}}{\mathrm{d}t} + \frac{\boldsymbol{v}}{\tau} = \frac{e}{m^*}\left(\boldsymbol{E}_{\mathrm{b}} + \frac{\boldsymbol{v}}{c} \times \boldsymbol{B}\right) . \tag{21}$$

In this equation $\boldsymbol{v}$ denotes the (ensemble-averaged) carrier velocity; m^* and τ are, respectively, the effective mass and mean scattering time of the charge carriers. For simplicity, we have assumed that they are scalars. Further refinements, such as a velocity dependence or time dependence of the parameters (to describe hot-carrier effects, for example) could be included in an ad-hoc fashion, but would preclude one from obtaining analytical expressions from these equations, which are their prime virtue. For the effective mass, we use the appropriate electron or hole band mass. The scattering time is introduced as a parameter to account for the mean time between the momentum-transfer collisions discussed in the previous subsection. Its physical origin does not need to be specified. It can account for carrier–carrier, carrier–phonon or carrier–impurity scattering, or a combination of these effects. It cannot, however, adequately account for intervalley scattering, which would lead to a change in the effective mass of the carriers.

The electric field $\boldsymbol{E}_{\mathrm{b}}$ and the magnetic field $\boldsymbol{B}$ experienced by charge carriers in (21) are, in general, functions of space and time. The spatial variation of the electric field is particularly relevant for devices in which currents flow perpendicularly to the surface of the emitter. The temporal variation of the bias field occurs only in the context of carrier-screening effects that arise for high excitation densities. This is the subject of Sect. 6 and will be neglected at present. For convenience, we also consider the fields to be spatially uniform. This is a well-justified assumption for the external bias fields in the lateral geometry. In the case of a surface-depletion field, it provides a qualitative description of the field if the thickness of the depletion layer exceeds the mean free path of electrons.

3.2.3 Response in the Absence of Magnetic Fields

Under the approximation of time-independent and spatially uniform driving fields, the solution to the equation of motion (21) is well known. The result is particularly easy to express in the Fourier-transform domain where we can write $\boldsymbol{v}(\omega) = \vec{\boldsymbol{\mu}}(\omega)\boldsymbol{E}(\omega)$. In the absence of an applied magnetic field, the mobility tensor is diagonal and has a value of

$$\mu(\omega) = \mu_{\mathrm{dc}} \frac{1}{1 - \mathrm{i}\omega\tau} , \tag{22}$$

with $\mu_{\mathrm{dc}} = \mathrm{e}\tau/m^*$.

In the time domain, the equivalent solution reads as

$$\mu(t) = \frac{\mu_{\mathrm{dc}}}{\tau} \mathrm{e}^{-t/\tau} \,. \tag{23}$$

With this carrier-mobility function in hand, we can express the current resulting from an arbitrary laser excitation pulse profile using the formalism developed above and expressed by (20). For the special case of instantaneous laser excitation at time t_0, the solution at time $t = t' + t_0$ is

$$\boldsymbol{j}(t, t_0) \sim \theta\,(t')\, \mathrm{e}^{-t'/\tau_{\mathrm{c}}} \left(1 - \mathrm{e}^{-t'/\tau}\right) \boldsymbol{E}_{\mathrm{b}} \,, \tag{24}$$

where we have assumed the carrier density to decay exponentially with a time constant of τ_{c}. This expression shows that the photocurrent rises exponentially towards the steady-state value with a time constant τ given by the carrier-scattering time. It simultaneously undergoes decay at an exponential rate determined by the carrier lifetime τ_{c}, corresponding physically to the reduction in the mobile carrier density with time.

3.2.4 Response in the Presence of a Magnetic Field

It is also interesting to consider the presence of a magnetic field, as will be discussed more extensively in Sect. 5. Within the Drude–Lorentz model we then obtain a nondiagonal mobility tensor relating the driving electric field and the velocity of the carriers moving in the semiconductor under the influence of the magnetic field. The results are most readily expressed in the frequency domain, from which the time-domain quantities can be obtained by Fourier transformation.

The result for motion in the presence of a magnetic $\boldsymbol{B} = B\hat{\boldsymbol{y}}$ is given by the following nonzero elements of the mobility tensor:

$$\begin{aligned}
\mu_{xx}(\omega) &= \mu_{zz}(\omega) = \mu_{\mathrm{dc}} \frac{1 - \mathrm{i}\omega\tau}{(1 - \mathrm{i}\omega\tau)^2 + (\omega_{\mathrm{c}}\tau)^2} \,, \\
\mu_{yy}(\omega) &= \mu_{\mathrm{dc}} \frac{1}{1 - \mathrm{i}\omega\tau} \,, \\
\mu_{xz}(\omega) &= -\mu_{zx}(\omega) = \mu_{\mathrm{dc}} \frac{\omega_{\mathrm{c}}\tau}{(1 - \mathrm{i}\omega\tau)^2 + (\omega_{\mathrm{c}}\tau)^2} \,.
\end{aligned} \tag{25}$$

Here the parameter $\omega_{\mathrm{c}} = \mathrm{e}B/m^*c$ denotes the cyclotron frequency of the carriers in the B field.

3.3 Predicted THz Waveforms and Spectra

We now examine some representative THz electric-field waveforms and spectra that result from application of the Drude–Lorentz model to generation by large-area emitters. We include only an electric bias field and do not consider

the influence of an applied magnetic field here. Figure 3a–d illustrates the behaviour for a typical carrier scattering time of $\tau = 300\,\text{fs}$ and carrier lifetimes of $\tau_c = 1\,\text{ps}$ and 100 ps. The results are obtained for the limit of an instantaneous laser excitation pulse. However, given the 300-fs scattering time, it is clear that the predictions would be essentially identical for laser pulses of 100 fs or shorter duration that are commonly used in current measurements.

The near-field amplitude shown in Fig. 3a corresponds directly to the transient current. Its rise time is determined by the scattering time of the carriers and it falls off on the time scale of the carrier lifetime. Clearly, the high-frequency part of the THz spectrum is controlled by the rise time of the photocurrent, as illustrated in Fig. 3c by the essentially identical behavior for the high-frequency response with 1 and 100 ps carrier lifetimes. The near-field THz spectrum will shift towards higher average emission frequency as the scattering rate increases, although this will be accompanied by an overall reduction in the signal strength. In this analysis, the carrier mass, if changed independently of the scattering time, would influence the overall magnitude of the emission, with light carriers giving a greater signal than heavy ones, but would not change the shape of the spectrum. The low-frequency part of the near-field response is, on the other hand, strongly influenced by the carrier lifetime. This is just the frequency-domain manifestation of the influence of the persistent electric field predicted for a long carrier lifetime.

The far-field time-domain waveforms are obtained as time derivates of the near-field waveforms. One of the apparent peculiarities is the nearly unipolar form of the waveform generated for the case of the 100-ps carrier lifetime. A unipolar form would, in fact, be inconsistent with Maxwell's equations. It would imply a nonzero time integral of the electric-field waveform, which in turn would yield a nonzero value for a radiated field at zero frequency. The resolution to this apparent conflict is simply that the far-field THz waveform has a weak, but long-lived negative tail. This behavior follows directly from the fact that the far-field electric-field waveform is calculated as the time derivative of the transient current. For a long carrier lifetime, this current will decrease very slowly and give rise to the weak, but persistent tail. The presence of the negative feature in the THz electric field is much more apparent for the short carrier lifetime of $\tau_c = 1\,\text{ps}$. Another feature to note in examining the far-field results is the blue shift that they exhibit compared to the near field. This is simply a result of diffraction of the THz radiation in the far field. Because of the derivative relation between the far- and near-field results, the far-field spectrum corresponds to the near-field spectrum multiplied by a factor of the frequency in the Fourier-transform domain.

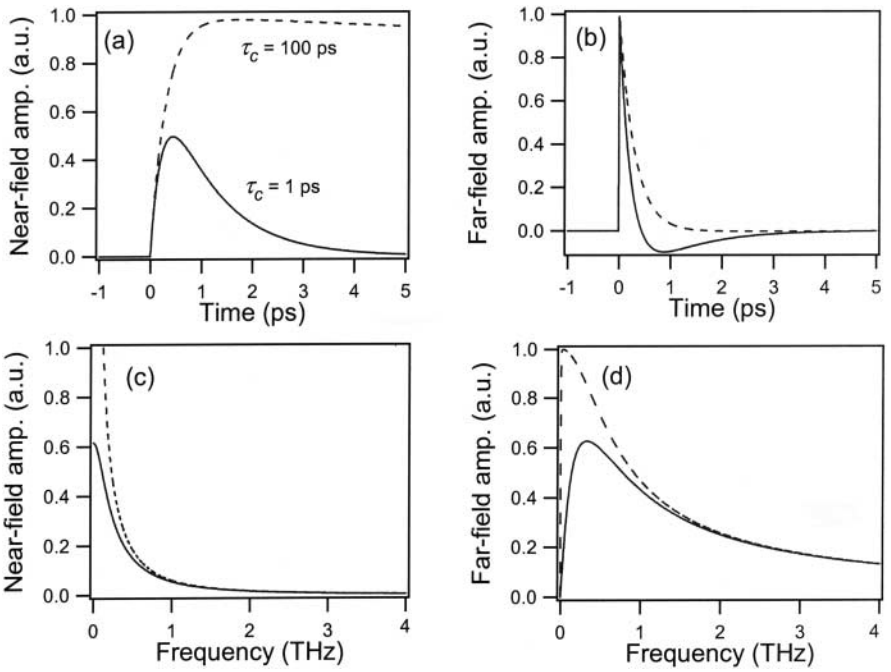

Fig. 3. (**a**), (**b**) Simulated electric-field waveforms for THz radiation from large-area photoconductive emitters in the near and far field based on the Drude–Lorentz model. (**c**), (**d**) The relative amplitude spectra of the THz waveforms in (**a**), (**b**). The excitation was assumed to be instantaneous and a carrier-scattering time of $\tau = 300$ fs was used. The *solid* and *dashed curves* correspond to carrier lifetimes of $\tau_c = 1$ and 100 ps

4 Basics of THz Radiation from Large-area Photoconductive Emitters

In this section, we review some of the key experimental observations and discuss their relation to the analysis of THz radiation from current transients presented above. We describe here results for devices with both bias fields along the plane of the surface and perpendicular to it. The general characteristics are similar in the two cases.

4.1 Directionality of THz Emission

One of the striking early observations for large-area photoconductive emitters was that the direction of the emitted radiation was controlled by the direction of the incident pump beam [30,33]. This behavior is, as mentioned in Sect. 2.1, readily understood in terms of a difference-frequency generation process. Nonetheless, the behavior distinguishes itself sharply from that for

traditional dipole emitters and other antenna structures in which the laser radiation only plays the role of triggering a spatially localized photoconductor [2]. Emission can occur in both the transmitted and reflected directions, as specified by the generalized form of Snell's law. With respect to the characteristics of these THz beams, their angular divergence is observed to be far greater [29] than that of the optical pump radiation. This situation is, however, a natural consequence of the much stronger diffraction effects for THz radiation that result from the much longer wavelengths involved.

The origin of the directionality of the THz emission lies in the transverse variation of the current transients. This property reflects, through the temporal sequence of the excitation, the angle of incidence of the pump radiation. It is for this reason that the emission direction can be changed by the direction of the pump beam. Several other schemes have also been introduced that are capable of controlling the direction and spatial characteristics of the emitted THz radiation by altering the transverse variation of the current transients. These include the use of a spatial light modulator to modify the intensity profile of the incident beam [43]. Also, a large-aperture emitter can be broken down into a set of smaller photoconductive emitters, each of which can be separately biased [44]. This permits the spatial properties of the emitted radiation to be controlled electrically.

4.2 Angular Dependence of the THz Emission Efficiency

Although the essential nature of the photocurrent transients does not depend on the angle of incidence of the pump optical radiation, as we have just seen, their relative timing across the transverse plane causes the THz emission direction to be defined along the appropriate reflected and transmitted directions. In addition, however, the direction of the incident beam has a significant impact on the *magnitude* of the emission. This dependence arises from two effects. One part is the variation in density of photogenerated carriers, as described through the familiar Fresnel factors for the optical radiation, with the angle of incidence of the pump laser. This effect tends to favor excitation near Brewster's angle with *p*-polarized optical pump radiation.

The second part, which may be much more significant, concerns the coupling efficiency of the current transients to radiated THz fields as a function of the direction of emission. We have examined this effect in Sect. 2. The case of THz emission from a transient current directed perpendicularly to the surface exemplifies these trends. For the normal direction no emission is possible, since the current flow has no component transverse to the emission direction. As shown in Fig. 2, the coupling efficiency increases sharply with increasing emission angle.

Figure 4, from the work of *Zhang* et al. [30], illustrates the strong predicted variation in the strength of the THz radiation. The figure shows the dependence of the transmitted THz radiation generated in the depletion region of an InP wafer as a function of the angle of incidence of the optical excitation

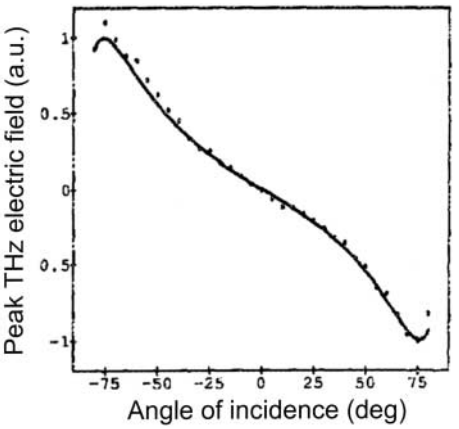

Fig. 4. Dependence of the peak electric field of the transmitted THz radiation generated by currents in the depletion field of an InP wafer as a function of the angle of incidence of the optical excitation as measured by *Zhang* et al. [30]. The *points* show the experimental data and the *solid line* is the predicted behavior

pulses. The measured THz field strengths (dots) were obtained by rotating the InP wafer along an axis perpendicular to the plane of incidence. A fixed, in position, dipole photoconductive antenna was used as the THz detector. The solid line was computed from the radiation formula for the transmitted THz radiation similar to (8), but with the consideration of the reflection loss of the excitation pulses.

4.3 THz Waveform and its Spectral Characteristics

The time-domain waveforms and spectral characteristics of THz radiation from large-area emitters have been the subject of much study. Here we highlight some of the key observations. The wide spectral bandwidth for emission from a large-area device excited by a short laser pulse is illustrated in the early data of *Greene* et al. [34]. In this measurement, detection was accomplished by means of a bolometer and spectral information was obtained using interferometry in the method so well developed in conventional Fourier-transform infrared spectroscopy. This detection approach has the advantage of providing an essentially unrestricted spectral bandwidth.

Figure 5 shows the results of such a measurement for an InP surface irradiated by a laser pulse of 120-fs duration. The spectral width of the response is seen, in this instance, to be comparable to that of the exciting laser pulse.

The details of the spectrum obviously reflect the various experimental parameters, including the duration of the excitation laser pulse and whether the measurement is made in the near field or the far field, the latter having a greater weighting of the high-frequency spectral components. In addition, the choice of photoconductive material and the nature of the bias field obviously are also critical parameters.

A more detailed view of the THz emission process is provided by the time-dependent THz electric-field waveforms. In Fig. 6 we show a comparison of the far-field THz waveforms originating from large-area photocon-

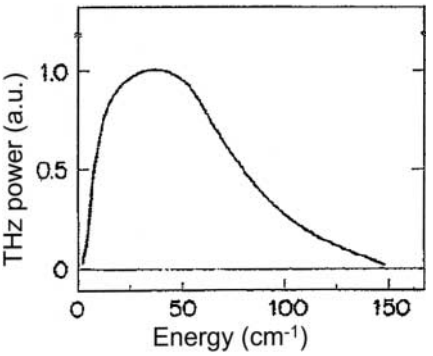

Fig. 5. Spectral characteristics of THz emission from a large-area InP emitter as determined using Fourier-transform detection by *Greene* et al. [34]

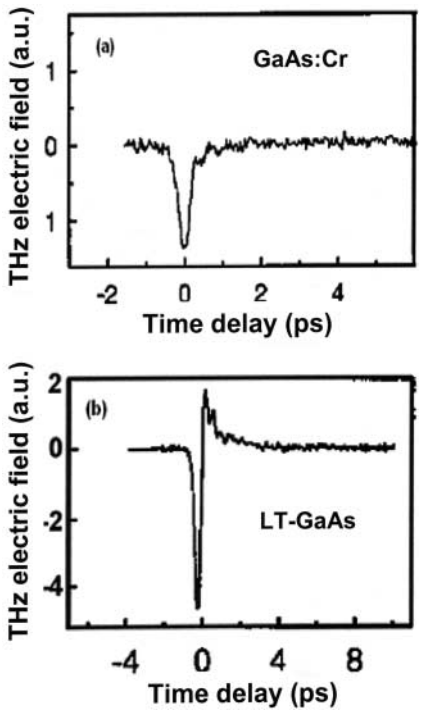

Fig. 6. Electric-field waveform of THz radiation emitted from (**a**) GaAs:Cr with a long carrier lifetime and (**b**) low-temperature-grown GaAs with a short carrier lifetime. The waveforms were measured in the far field with electro-optic sampling by *Kuzel* et al. [45]

ductive emitters in a medium with (a) GaAs:Cr with a long carrier lifetime and (b) low-temperature-grown GaAs with a short carrier lifetime from the work of *Kuzel* et al. [45]. These waveforms were measured using electro-optical sampling, which was verified to provide sufficient bandwidth to avoid distortions in the recorded signal. The electric-field waveforms show a largely unipolar shape for the radiation from the GaAs:Cr emitter. This result is in good agreement with the predictions of Sect. 3. The far-field THz waveform should be proportional to the time derivative of the current. If the current

falls sufficiently slowly, it should have a unipolar derivative, corresponding to the rise and leveling off of the current transient, as seen in the simulation of Fig. 3b. For the low-temperature-grown GaAs emitter, the carrier lifetime is known to be quite short. Then we expect the current transient to drop off relatively sharply. The rise and fall of the current transient yield a bipolar signal, as observed experimentally in Fig. 6b and in the simulation of Fig. 3b. In practice, few of the waveforms found experimentally are as clean and easy to understand as those of Fig. 6. Departures from the simple theory may reflect added physical processes, such as saturation effects. Perhaps more common, however, is the influence of spectral distortions induced by optical components and the finite bandwidth of the detection system.

4.4 Dependence on the Bias Fields

The THz field is proportional to the transient current. Within the elementary model of carrier transport considered in Sect. 3, the current for constant photoexcitation will be proportional to the strength of the bias field. Hence, the THz field should increase in direct proportion to the strength of the bias field. In fact, such an analysis neglects the possible role of high-field mobility effects, as well as effects related to the finite size of the drift region. Such corrections may be important for the depletion-field emitters, where very high effective bias fields are achieved over short length scales. For the large-aperture emitters based on transverse fields, these effects are expected to be less significant given the more modest field strengths and the large spatial dimensions involved.

Experimental measurements for the scaling of the THz field with the bias field strength have indeed been reported for such large-aperture emitters [46,47]. Figure 7, from the work of *Benicewicz* and *Taylor* [46], shows the observed dependence of the peak THz radiation on the bias field for various excitation conditions. No deviation from the linear dependence was observed for bias fields up to 12 kV/cm, the maximum field strength attainable without complications from breakdown effects.

4.5 Power Scaling of Large-area THz Emitters

The scaling of large-area photoconductive emitters with the fluence of optical excitation pulses was one of the issues that attracted early attention. It was first investigated by *Darrow* et al. [48] in a GaAs large-aperture emitter and later more comprehensively by *Taylor* and collaborators [37,46,49]. To understand the interest in this aspect of THz emitters, it is important to recall that the THz generation process is inherently nonlinear. In the low-fluence regime, one has a linear relationship between the optical laser *intensity* and the emitted THz *electric field*. This relation implies, of course, as one would expect for a second-order nonlinear interaction, a quadratic relation between the optical pump power and the corresponding THz power. Consequently,

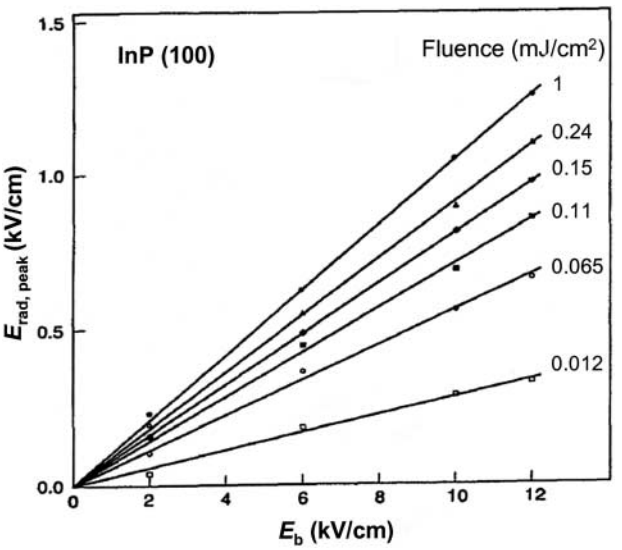

Fig. 7. Dependence of the peak electric field of THz radiation from a large-aperture InP emitter on the bias field for various laser excitation fluences as reported by *Benicewicz* and *Taylor* [46]. A linear variation is observed under all conditions, as expected within the simple theory of THz emission

even with the availability of a sample surface of arbitrarily large dimensions, to attain the maximum possible conversion efficiency, one always wishes to focus the pump laser beam as tightly as possible, that is up to the point where saturation or damage effects intervene. It is for this reason that a complete understanding of saturation effects is critical to optimizing the efficiency of a THz emitter and thus the maximum THz power attainable with a laser pump beam of specified characteristics.

Figure 8 illustrates the typical situation observed experimentally. The symbols show the peak values of the THz radiation measured in the far field as a function of the optical excitation fluence for several bias fields of a large-aperture emitter. As expected, at low excitation fluence, the radiated field increases linearly with the excitation fluence. However, the radiated THz field clearly saturates at high excitation fluence. This effect can be understood as the result of screening of the bias field. We return to a more complete discussion of this phenomenon in Sect. 6.

4.6 Other Mechanisms of THz Emission from Semiconductors

The focus in our discussion has been the role of photogenerated current transients as the source of THz emission. While this is the dominant mechanism in certain regimes, it is not the only mechanism. Indeed, for particular excitation conditions, such current transients are clearly unimportant. This would

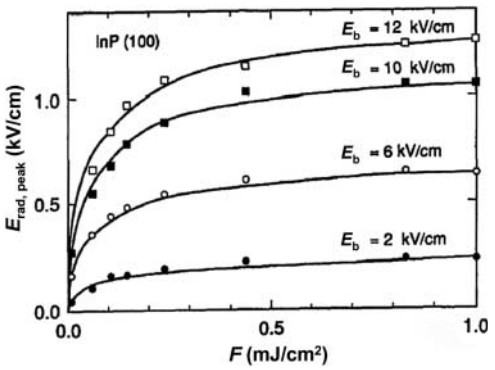

Fig. 8. Peak strength of the radiated THz waveform in the far field versus the fluence F of the optical excitation pulses for various bias fields E_b in an InP large-aperture photoconductive emitter. The *solid curves* are fits of the saturation theory described in Sect. 6 to the data. (After the results of *Benicewicz* and *Taylor* [46])

be the situation for below bandgap excitation (in the absence of two-photon absorption). Even for above bandgap excitation, the current-surge processes compete with other possible generation schemes. Such competing mechanisms may be identified using geometries that, as discussed above in Sect. 2, cannot give rise to emission through transient currents. Principal among these are normal emission for a bias field perpendicular to the interface and emission in the orthogonal polarization for in-plane bias fields.

Two classes of alternative generation mechanisms have been discussed in the literature, both of which correspond to an (essentially) instantaneous material response. One possibility is simply the nonresonant second-order nonlinear response expected in any noncentrosymmetric semiconductor, such as the III–V materials. This effect, which is often termed optical rectification, can be identified by the distinctive dependence that it shows on the crystallographic orientation of the sample. Since saturation of this process is not expected from screening effects, its relative prominence is expected to increase with increasing fluence of the pump laser. Figure 9, from the work of *Saeta* et al. [50] illustrates the variation of THz emission intensity from an InP(001) sample as it is rotated about its surface normal. Within the model of a photocurrent transient moving in the depletion region, as discussed above, no *s*-polarized (TE) radiation would be expected. In fact, *s*-polarized radiation is observed and its distinctive angular dependence matches precisely the form predicted from the second-order nonlinearity of the sample. For the case of THz *p*-polarized (TM) emission, a contribution from a current transient is allowed. However, the observed dependence on sample orientation requires one to invoke an additional mechanism as well.

The optical rectification process, we note, has been widely developed for THz generation, typically in materials with a completely nonresonant response. The advantage of such an approach is the inherent speed of the response, which may be viewed as essentially instantaneous. The disadvantage of such an approach is the relative weakness of the nonlinear response. Thus, in order to obtain significant THz emission via the optical rectification mech-

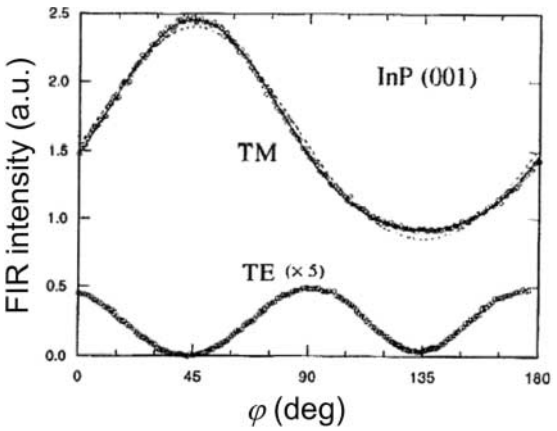

Fig. 9. *p*-polarized (TM) and *s*-polarized (TE) THz intensity measured for excitation of an InP(001) wafer by 100-fs *p*-polarized laser excitation pulses at 2 eV photon energy. The response is shown for oblique laser excitation as a function of rotation of the wafer about its surface normal. The *s*-polarized radiation arises purely from the nonresonant second-order nonlinearity and varies with the rotation angle as $\sim \cos^2(2\varphi)$. The *p*-polarized component includes both an optical rectification and a transient-current contribution. (After the results of *Saeta* et al. [50])

anism it is desirable to use a medium of appreciable thickness. This in turn leads to the necessity of considering phase-matching constraints. While various approaches exist for difference-frequency mixing in the far-infrared or for the generation of a particular far-infrared frequency through optical rectification [51,52], the problem of broadband phase matching is a challenging one [53].

A second mechanism for THz generation is that of an electric-field-induced second-order nonlinearity, an effect analogous to the familiar field-induced second-harmonic generation process. This process, unlike the usual second-order nonlinearity, is not restricted to noncentrosymmetric media. In terms of nonlinear optics it can be considered as a third-order response, which is permitted in centrosymmetric materials. This process has been discussed primarily in the context of a below bandgap excitation. In this context it has been termed a virtual photoconductivity process [50,54,55,56,57].

We should also remark that the description that we have given of the transport of photocarriers has been essentially based on bulk-like properties. In semiconductor heterostructures of sufficiently small spatial dimension, quantization effects for perpendicular motion of the carriers may become significant. Under these conditions, THz emission may be strongly influenced by the intersubband spacing or the miniband width of the Bloch superlattices. Examples of THz radiation observed from such heterostructures include that associated with coherently oscillating electrons in double-well potentials

observed by *Roskos* et al. [39]; the emission from oscillations of excitons in a quantum well [40]; and THz emission from Bloch oscillations [41].

5 Influence of Magnetic Fields

In Sect. 4, we saw that THz radiation from large-area emitters with bias fields perpendicular to the surface vanishes for optical excitation at normal incidence. This is a direct consequence of the transverse nature of electromagnetic waves: A current transient flowing parallel to the direction of radiation cannot radiate. Therefore, any alternation of the direction of the current can be expected to strongly influence the THz radiation. One convenient means to alter current direction is to use the Lorentz force provided by an external static magnetic field. Indeed, as we discuss in the present section, external magnetic fields can not only turn on otherwise forbidden THz emission, but also significantly enhance the THz emission strength even when the process is allowed by symmetry. Furthermore, in the case of a magnetic field of sufficient strength to induce fully developed cyclotron orbits, a significant change in the spectral characteristic of the THz radiation has been observed. The essential elements of these various effects can be understood using the model developed above, i.e., a combination of radiation from a current sheet and carrier dynamics described within the simple Drude–Lorentz picture.

5.1 Switching of THz Emitters using Magnetic Fields

As early as 1993, the possibility of altering and enhancing the THz emission from photoconductors by application of an external magnetic field was demonstrated by *Zhang* et al. [58,59]. In these investigations, the researchers studied the transmitted THz radiation from a GaAs wafer illuminated by femtosecond laser pulses at normal incidence. The THz radiation observed in the forward direction as a function of the strength of an in-plane magnetic field is shown in Fig. 10. The THz radiation clearly could be switched on and off by the application of an external magnetic field. The amplitude of the radiated THz field was observed to vary linearly with magnetic fields up to $\sim 0.2\,\mathrm{T}$, with the waveform changing its polarity with switching of the sign of the magnetic field.

5.2 Enhancement of THz Radiation in Magnetic Fields

The phenomenon of the influence of magnetic fields on THz emission was the subject of several ensuing investigations. Enhancements in the THz power of nearly a factor of 100 were reported. In addition, measurements characterized many features of the field-induced enhancement, including its dependence on the strength and orientation of the magnetic field [36,58,59,60,61,62,63,64,65], [66,67,68,69], on the excitation geometry and laser photon energy [70,71], on

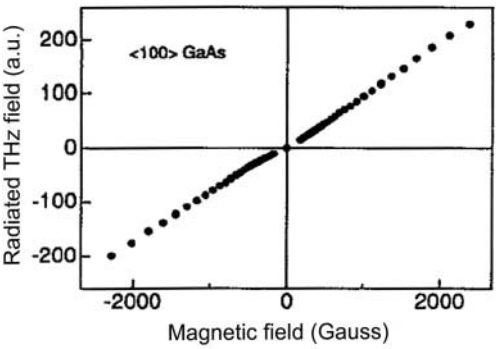

Fig. 10. An early demonstration reported by *Zhang* et al. [58] of the possibility of switching THz emission on and off by the application of a magnetic field. In this measurement a GaAs wafer was illuminated at normal incidence by femtosecond laser pulses to produce a current transient in the depletion region of the sample

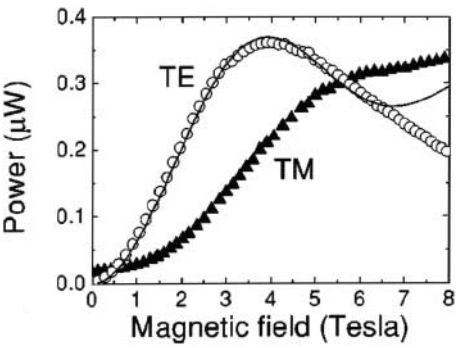

Fig. 11. THz radiation from (100) GaAs as a function of the applied magnetic field at a temperature of 200 K reported by *Corchia* et al. [69]. The *circles* and *triangles* represent, respectively, the *p*-polarized (TM) and *s*-polarized (TE) THz power. The magnetic field lies in the plane of incidence and is perpendicular to the direction of the optical excitation beam

the excitation density [68,69], on the choice of the photoconductive material [36,62], and on the temperature of the emitter [63,64,65,66,67]. Most of these parameters had a significant influence on the degree of enhancement in the THz emission.

Figure 11 displays a representative result for the enhancement of the THz emission versus magnetic-field strength for photoconductive emission from the depletion field of a GaAs wafer. In these studies by *Corchia* et al. [69], magnetic fields with strengths up to 8 T were applied in the plane of incidence in the direction perpendicular to the optical beam. Without a magnetic field, only *p*-polarized (TM) THz emission was observed. With the application of the external magnetic field, the *p*-polarized THz emission increased sharply. At the same time, a significant *s*-polarized component appeared. The power in both components grew approximately quadratically, in accord with a linear variation of the THz *field strength* described in Fig. 10 above. For relatively weak magnetic fields, no significant distortion of the spectral density of the THz emission was observed. At sufficiently high magnetic field strengths, the enhancement of the emitted THz power showed a clear saturation.

5.3 Origin of THz Enhancement in Magnetic Fields

With respect to the mechanism of the observed magnetic-field enhancement, the initial report [58,59] already identified the possible role of the Lorentz force in altering the current transient and, hence, the THz emission. Only recently, however, has the Drude–Lorentz model been actually considered in a more detailed fashion and used to make specific predictions of possible enhancements in THz emission [36,67,68,72]. With appropriate treatment of the THz radiation problem, this simple model has been found to be adequate to describe the key features of the enhancement and to provide semiquantitative agreement with the experimental results. The key idea in this explanation is that the high dielectric constant of typical photoconductive materials at THz frequencies causes the radiation efficiency of current transients flowing along the direction of the surface to far exceed that of currents flowing perpendicular to the surface. Thus, while the Lorentz force associated with the magnetic field does not lead to a larger *magnitude* of acceleration for the carriers, it bends the current into a *direction* that radiates more efficiently. Similarly, the idea of maximizing the component of the current perpendicular to the direction of radiation has been exploited in an epitaxial InAs emitter grown on a GaAs prism [73]. The addition of the prism, also having a large dielectric constant for THz radiation, permits the direction of the THz radiation in the InAs layer to be relatively far from the surface normal. This was shown to lead to an increase in the radiation efficiency by a factor of ~ 20.

5.3.1 THz Radiation in Magnetic Fields Within Drude–Lorentz Model

For simplicity, we examine only the far-field solution for the radiated THz emission. The qualitative behavior of the phenomena is similar in the near field. We further assume that the laser pulse duration $\ll$ carrier scattering time $\ll$ carrier lifetime. These relations will generally be valid for sufficiently short pump laser pulses. These assumptions are introduced for the sake of clarity and simplicity and their relaxation would not significantly alter the trends discussed in this analysis. Within these assumptions, the THz electric field in the far-field zone is simply proportional to the carrier acceleration.

Additionally, we treat the electric bias field and the external magnetic field as time-independent and spatially uniform. This assumption is completely valid for the magnetic field. For the electric field, a time-independent approximation is valid provided that the injected carrier density is sufficiently low to avoid screening effects, a regime that can be readily identified experimentally by the linearity of the THz field with the pump-laser fluence. The assumption of a spatially uniform electric field is obviously a simplification of the true nature of a surface depletion or accumulation field. The qualitative results are, however, expected to be similar. In the limit where the carrier scattering length is short compared to the width of the surface depletion/accumulation region, the approximation of a uniform bias field will

be relatively accurate. The advantage of introducing these approximations is that the problem then has a simple analytical solution for the carrier dynamics and, hence, for the THz radiation fields.

The carrier acceleration can be obtained either by solving the Drude–Lorentz equation of motion (21) or through the use of the mobility tensor (25) (Sect. 3) for a bias electric field of $\boldsymbol{E}_\mathrm{b} = E_\mathrm{b}\hat{\boldsymbol{z}}$ lying perpendicular to the surface plane of the sample. We see that a magnetic-field component of $\boldsymbol{B}$ lying parallel to $\boldsymbol{E}_\mathrm{b}$ has no effect on the motion of the carriers starting from rest. We therefore restrict our analysis to configurations with $\boldsymbol{B}\perp\boldsymbol{E}_\mathrm{b}$.

Let us first consider the magnetic field to lie along the intersection of the plane of incidence and the surface plane ($\boldsymbol{B} = B\hat{\boldsymbol{x}}$). The equation of motion can then be solved for the appropriate initial condition of $\boldsymbol{v}(t = 0) = 0$ to yield a carrier acceleration of

$$\boldsymbol{a}(t) = eE_\mathrm{b}/m^*\mathrm{e}^{-t/\tau}\left[-\sin(\omega_\mathrm{c}t)\hat{\boldsymbol{y}} + \cos(\omega_\mathrm{c}t)\hat{\boldsymbol{z}}\right], \tag{26}$$

where $\omega_\mathrm{c} = eB/m^*c$ is the cyclotron frequency, as defined above in conjunction with (25). The two components of the radiated THz electric field in the far-field zone are thus

$$\begin{aligned} E_\mathrm{s}(t) &\sim \theta(t)\mathrm{e}^{-t/\tau}\sin(\omega_\mathrm{c}t)\frac{1}{\cos\theta + \sqrt{\varepsilon - \sin^2\theta}}, \\ E_\mathrm{p}(t) &\sim \theta(t)\mathrm{e}^{-t/\tau}\cos(\omega_\mathrm{c}t)\frac{\sin\theta}{\varepsilon\cos\theta + \sqrt{\varepsilon - \sin^2\theta}}. \end{aligned} \tag{27}$$

From these relations, the initial experimental observation of switching THz emitters by magnetic fields can be readily explained. At normal incidence, the p-polarized radiation vanishes identically because of the presence of the geometrical factor of $\sin\theta = 0$. In the absence of magnetic fields, the s-polarized radiation is also zero, since $\sin(\omega_\mathrm{c}t) = 0$. When a magnetic field is applied, however, an s-polarized component of the THz field is produced. This radiation arises because the magnetic field induces a component of motion along the y-axis, which can couple to radiation emerging perpendicular to the sample surface.

For weak magnetic fields, where the dimensionless parameter $x \equiv \omega_\mathrm{c}\tau = \mu_\mathrm{dc}B \ll 1$, we may use $\sin(\omega_\mathrm{c}t) \approx \omega_\mathrm{c}t$, since the emission lasts only for a time of the order of the scattering time τ. The radiated field amplitude is thus linearly proportional to the cyclotron frequency, or equivalently, to the strength of the magnetic field. For GaAs at room temperature, a magnetic field strength of 0.2 T corresponds to $x = 0.1$ (taking the mobility to be that of the bulk semiconductor), for which the linear relation holds reasonably well. Thus the linearity of the THz field strength displayed in Fig. 10 above is precisely what one would expect. The switching of the polarity of the THz waveform with the polarity of magnetic fields is not, however, restricted to this regime of weak magnetic fields discussed here. It holds generally because

the acceleration associated with the magnetic field is an odd function of the magnetic field.

Another interesting geometry that is frequently used corresponds to an applied magnetic field perpendicular to the plane of incidence $\boldsymbol{B} = B\hat{\boldsymbol{y}}$ (Faraday geometry). We find the acceleration for this case to be

$$\boldsymbol{a}(t) = eE_{\mathrm{b}}/m^{*}\mathrm{e}^{-t/\tau}(-\sin\omega_{\mathrm{c}}t\hat{\boldsymbol{x}} + \cos\omega_{\mathrm{c}}t\hat{\boldsymbol{z}})\,, \tag{28}$$

and the far-field THz emission to be

$$\begin{aligned} E_{\mathrm{s}}(t) &\equiv 0\,, \\ E_{\mathrm{p}}(t) &\sim \theta(t)\mathrm{e}^{-t/\tau}\left[\cos(\omega_{\mathrm{c}}t) + \gamma\sin(\omega_{\mathrm{c}}t)\right]\frac{\sin\theta}{\varepsilon\cos\theta + \sqrt{\varepsilon - \sin^2\theta}}\,. \end{aligned} \tag{29}$$

Unlike the previous case, the s-polarized radiation is absent even in the presence of a magnetic field. Inspection of (29) also makes clear the significant role in the THz enhancement played by the radiation efficiency factor $\gamma = \sqrt{\varepsilon - \sin^2\theta}/\sin\theta$. As can be seen from (28), the application of the magnetic field does not change the magnitude of the acceleration, $|\boldsymbol{a}|$. It does, however, convert some of the current initially flowing along the surface normal ($\hat{\boldsymbol{z}}$) into a component parallel to the surface ($\hat{\boldsymbol{x}}$). The latter, according to (29), then radiates γ times more efficiently than the former. Since $\gamma \gg 1$ for typical photoconductive materials (with $\varepsilon \gg 1$), THz emission is significantly enhanced by the application of a magnetic field.

In the case of an arbitrary orientation of the magnetic field, we note that the emitted THz radiation can have both p- and s-polarized components. In the following discussion, which mirrors the treatment of [36,62], we concentrate on the second geometry with the applied magnetic field oriented perpendicular to the plane of incidence to emphasize the role of radiation-coupling effects.

5.3.2 Magnetic-Field-Induced Power Enhancement

In the limit of weak magnetic fields, since the changes in the spectral density of the radiation are not very great, we focus on the magnetic-field-induced change in the total emitted power. We do this by introducing a power-enhancement factor defined as

$$\eta_{\mathrm{P}} = \frac{\int_{-\infty}^{+\infty}\mathrm{d}t\,|E_B(t) - E_{B=0}(t)|^2}{\int_{-\infty}^{+\infty}\mathrm{d}t\,|E_{B=0}(t)|^2}\,. \tag{30}$$

Note that this factor has been constructed so that $\eta_{\mathrm{P}} = 0$ (not 1) when $B = 0$. From (29), we then obtain for the power-enhancement factor the following

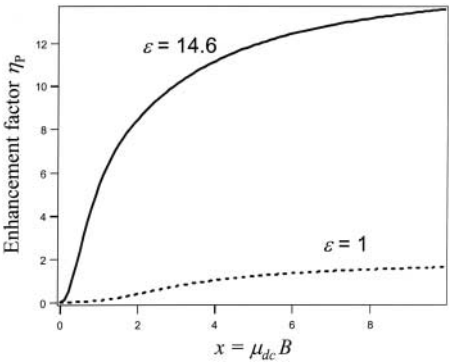

Fig. 12. The magnetic field enhancement factor η_{P} as a function of the dimensionless magnetic-field strength $x = \mu_{\mathrm{dc}}B$ calculated from the model described in the text. The *solid line* corresponds to an InAs emitter with its usual dielectric constant of $\varepsilon = 14.6$ excited at 45 °. The *dotted line* is the result for the same geometry but with $\varepsilon = 1$

expression:

$$\eta_{\mathrm{P}}(\gamma, x = \mu_{\mathrm{dc}}B) = \frac{\gamma^2}{2} + \frac{3}{2} + \frac{1 - \gamma^2 + 2\gamma x}{2(1 + x^2)} - \frac{2 + \gamma x}{1 + x^2/4}\,. \tag{31}$$

This quantity is thus determined solely by the radiation factor γ and the dimensionless magnetic-field-strength parameter $x \equiv \omega_{\mathrm{c}}\tau = \mu_{\mathrm{dc}}B$.

As an example of the behavior of the model, we show in Fig. 12 the enhancement predicted for an InAs emitter excited by pump radiation incident on the sample at 45 °. A strong enhancement is predicted for the tabulated value of the THz dielectric constant of $\varepsilon = 14.6$ (solid line). However, very little effect is expected under the same circumstances for a hypothetical material with $\varepsilon = 1$ (dotted line). In the latter case, the wavevector of THz radiation inside the material is no longer close to the surface normal, so that the influence of the magnetic fields in increasing the radiation efficiency is minor.

The asymptotic behavior of the enhancement as a function of the magnetic-field strength emerges readily from (31) and is clearly seen in Fig. 12. In the regime of weak magnetic fields ($|x| \ll 1$), the enhancement is quadratic in the magnetic-field strength, with $\eta_{\mathrm{P}} \approx (\gamma\mu_{\mathrm{dc}})^2 B^2/2$. For strong magnetic fields, the enhancement saturates at $\eta_{\mathrm{P}} = \gamma^2/2 + 3/2$, a value that depends on the optical properties of the material, but, interestingly, not on the carrier mobility. Saturation occurs in the range of $|x| \gg x_{\mathrm{s}} \approx 6/\gamma$ or $B_{\mathrm{s}} \approx 6/\gamma\mu_{\mathrm{dc}}$. Thus materials with higher carrier mobilities will, in some sense, show more favorable properties: they will reach the same saturation magnetic-field enhancement, but will do so at a lower applied magnetic field.

5.3.3 Angular Dependence of the Power Enhancement

Examination of the angular dependence of the THz emission provides a means of isolating the radiation-efficiency effects that are predicted to lie at the heart of the enhancement mechanism of the THz emission. The issues related to

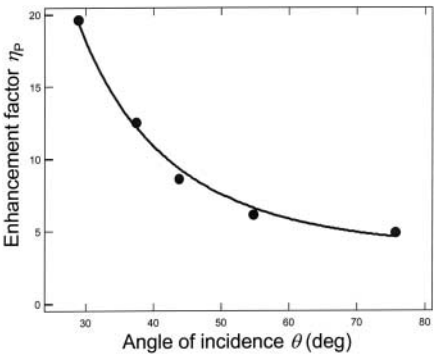

Fig. 13. Experimental data for the angular dependence of the THz power enhancement factor η_P for a (100) InAs sample under a magnetic field strength of 1 T (*filled circles*). The *solid line* corresponds to a fit to the model presented in the text. (After *Shan* et al. [36])

carrier dynamics and the details of motion in the depletion region will be essentially identical for the different geometries. However, for different angles of incidence, the relative coupling efficiency of the two orthogonal components of the current (J_x and J_z) will clearly vary. This will in turn be reflected in the magnetic-field enhancement.

Figure 13 shows the angular dependence of the (unsaturated) enhancement for an InAs emitter under a magnetic field of $B = 1\,\mathrm{T}$ perpendicular to the plane of incidence. The enhancement exhibits a strong dependence on the angle of incidence, θ, of the pump radiation. The experimental data from [36], shown as filled circles on the plot, agree very well with a fit of the model (solid line). The only adjustable parameter in this fit is the carrier mobility. In the limit of $\varepsilon \gg 1$, the theory actually predicts a universal angular dependence given by $\eta_P \propto \gamma^2 = \left|\varepsilon - \sin^2\theta\right| / \sin^2\theta \sim 1/\sin^2\theta$. Such behavior has, in fact, been observed in several other III–V material systems [36].

5.4 Cyclotron Radiation

In the presence of weak magnetic fields with $x \ll 1$, as just discussed, the spectrum of the THz emission is not expected to change dramatically. The main effect of the magnetic field is to induce a slightly deflected direction of the photocurrent with a high radiation coupling efficiency. With increasing field strength, we see from (29) that the THz radiation will begin to approximate transient cyclotron emission, with a peak at the cyclotron frequency ω_c and a spectral width determined by the scattering rate $1/\tau$. Indeed, such peaks have been identified by *Some* and *Nurmikko* [63,70] in their studies of GaAs epilayers and modulation-doped heterostructures at liquid-helium temperatures. The low-temperature regime is needed to increase the value of the scattering time τ (or, equivalently, of the mobility), so as to enter the regime where the dimensionless magnetic field strength $x \gg 1$.

Figure 14a shows a series of THz waveforms measured by *Some* and *Nurmikko* [63] from an undoped GaAs epilayer at $T = 5\,\mathrm{K}$ as a function of the

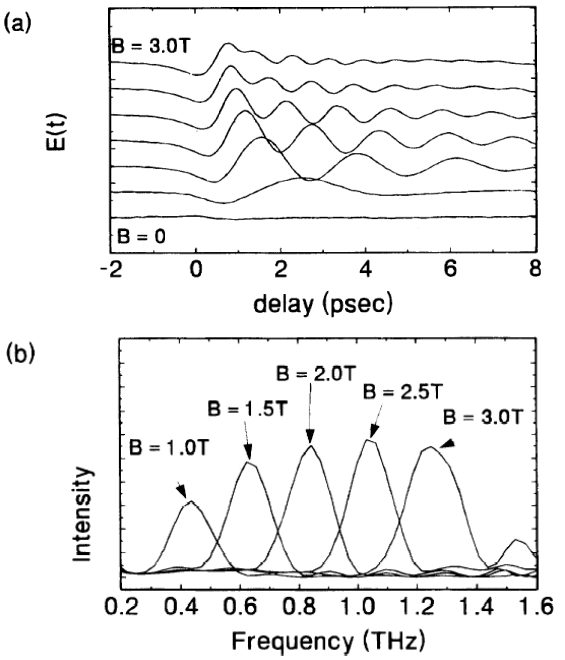

Fig. 14. Data of *Some* and *Nurmikko* [63] showing time-domain waveforms for a THz emitter under the influence of an external B field and the corresponding power spectra. The influence of the cyclotron resonance is clear in these data taken on low-temperature samples, with their associated low scattering rates and high values of the dimensionless magnetic-field strength x

magnetic-field strength up to a value of 3 T. In this measurement, the magnetic field is applied parallel to the direction of propagation of the irradiating laser beam, which is incident on the sample at an angle of 25 °. In Fig. 14b the corresponding power spectra are presented. Each spectrum is dominated by a single peak that shifts linearly with the magnetic field strength and can be identified with the cyclotron frequency ω_c. The effective mass deduced from the data is $0.068\, m_0$, which is consistent with the accepted electron band mass of GaAs. A scattering time of ~ 5 ps of the electrons was obtained by fitting the measured oscillations in the time-domain waveforms to an exponentially damped sinusoidal form $E(t) \sim \theta(t) \mathrm{e}^{-t/\tau} \cos \omega_c t$.

5.5 Refinements Beyond the Drude–Lorentz Model

The simple Drude–Lorentz model described above explains the strong dependence of the magnetic-field enhancement factor observed experimentally on the angle of emission of the THz radiation. The model predicts the dependence of the enhancement on the strength of the applied magnetic field. In particular, the observed low-field dependence of the enhancement and the

existence of a saturation effect emerge naturally from this treatment. It also predicts the presence of cyclotron-resonance emission in the regime of large magnetic-field strengths of $x = \omega_c \tau = \mu_{dc} B > 1$ and qualitatively describes well the characteristic features of these spectra. Nonetheless, for better quantitative agreement, improvements in the treatment of the carrier motion are warranted. Some of the missing ingredients of a complete discussion would include, to name a few, the role of the motion of holes, the influence of ballistic carrier motion, the effect of the spatial variation of the depletion field, particularly for samples with narrow depletion regions, high-field mobility effects, and the influence of carrier–carrier screening. Indeed, recent studies indicate that carrier–carrier interaction in the form of coupled cyclotron-plasma excitations may play an important role in the THz emission [67]. To incorporate this wide range of possible additional effects to achieve improved quantitative agreement with experiment in various regimes, an approach based on simulation of the carrier dynamics, such as the Monte Carlo approach of [74], may be necessary.

At high carrier excitation densities, the ultrafast variation of the bias field on the time scale relevant for THz radiation also becomes important. As we discuss in the next section, this effect leads to screening and saturation of the THz emission with increasing pump laser fluence. Interestingly, experiments by *Corchia* et al. [69] have shown that the application of an external magnetic field may act to increase the saturation fluence of the optical excitation pulses, thus further improving the THz emission efficiency. This effect has been attributed [69] to a decrease in the degree of the screening of bias fields during the first ~ 1 ps after photoexcitation, the time period most essential for THz emission, as a consequence of the altered motion of the carriers in the presence of the magnetic field. In the next section, we turn to the question of the dynamics of bias fields and saturation effects.

6 Dynamics of Bias Field

In our discussion up to this point, we have considered the electric bias field that induces the photocurrent transient to be time independent and uninfluenced by the presence of the photocarriers. This approximation is valid as long as the induced change of the bias field is slight, or, more correctly, the change of the bias field is slight during the period of time relevant for the THz emission process, typically ~ 1 ps after photoexcitation. Clearly for sufficiently low excitation densities, this approximation is valid. With increasing excitation density, however, this approximation will necessarily break down and the back action of the carriers on their own motion must be considered. This effect will generally lead to a reduction in the effective strength of the bias field and a concomitant decrease in the efficiency of THz generation. In addition to the inherent interest in understanding such field dynamics, these bias-field screening effects are of key importance for the generation of intense

THz radiation. The reader should recall that the THz generation process is inherently nonlinear. The emitted THz field scales, neglecting saturation effects, quadratically in the field of the exciting laser. Thus, the optimum conversion efficiency of optical radiation into THz radiation will occur at the highest allowable excitation density, just as for other nonlinear conversion processes such as second-harmonic generation. It follows that in the absence of saturation effects, the power of THz radiation generated by a laser pulse of given energy will increase as the laser beam is focused more tightly. The limitation for this procedure is the emergence of saturation effects at sufficiently high excitation densities.

Generally speaking, the back action of the motion of the photogenerated carriers on the bias field reflects both the charge distributions that the carriers create and the associated currents. While the charge and current distributions are obviously intertwined, it is often convenient to divide the effects into two limiting cases associated with each of them separately. The former arises from spatial separation of the photogenerated electron–hole pairs and is termed space-charge screening; the latter, termed near-field screening by the THz radiation field, is just the back action of the THz emission field on the photocarriers. Analogous considerations would apply for induced changes in any applied magnetic bias fields. Such effects would be relevant in the context of the role of photocurrents, since these are the source of magnetic fields. Given the relative strength of the near-field THz magnetic fields and the scale of the applied magnetic fields, these effects would normally be expected to be minor, however, and will not be considered further.

Before proceeding with a detailed discussion of these screening effects, we first would like to give a qualitative description of the processes of space-charge and THz near-field radiation screening, emphasizing their relative importance for different types of emitters. We first describe the space-charge effect. Under the influence of the electric bias field, the photogenerated electrons and holes drift in opposite directions. In a completely homogeneous medium with homogeneous excitation of the photocarriers, this motion of the charge carriers will only result in the generation of a current; no space charge will develop. For a spatially *inhomogeneous* system, however, charge separation does occur. In a simple electrostatic picture, which is relevant for charge separation on short length scales, the build-up of the space charge can continue, for a sufficient density of photogenerated carriers, until the initial bias field is completely screened. Thus, it is clear that the effect of space charges can be quite significant. With respect to the generation of THz radiation, one must consider, however, not only the ultimate *magnitude* of the space-charge screening, but the *dynamics* of the creation of this field. For a charge separation occurring over large distances, both the time lag for the creation of the space charges and the retardation effects in their influence on the carriers in the system become relevant. If the screening of the bias field develops only after the period of emission of the THz radiation has ended,

then this effect is obviously inconsequential in terms of the properties of THz emission.

From these considerations, it is apparent that space-charge screening for large-area photoconductive emitters will be much more significant when the current flow is in the direction perpendicular to the surface, rather than parallel to it. In the former case, the spatial scale over which charge transport occurs and over which charges may build up is small. It may be governed by the width of the depletion field or the physical dimensions of different materials in p–i–n structures or engineered heterostructures. Depletion fields, for example, typically extend only over a fraction of a micrometer. Given this short length scale, propagation times for electromagnetic fields are negligible and the problem is essentially electrostatic in character. For *lateral* current flow in such a large-area device, however, the situation is quite different. In the region of homogeneous excitation of the material (in the presence of a uniform bias field), no net charge develops and no space-charge effects need to be considered. Only at the boundaries of this homogeneous region, which may be separated by an appreciable distance, does space charge develop. In considering the influence of such space charges, one must then allow for appropriate time delays. Both the finite time for charge transport to occur and the finite time for this effect to act back on the main part of the emitter, as controlled by retardation effects, are relevant. The consequence of these observations is that large-area emitters with lateral currents are much less affected by space charges than emitters with currents flowing perpendicular to the surface. In the former case, simple consideration of retardation effects indicates that the main part of the THz emission process, occurring within ~ 1 ps, cannot be influenced by space charges if the length scale of the active area is ~ 1 mm or larger. However, for smaller gap spacings of say, 50 μm, these effects can develop to a significant degree on the time scale of the initial THz emission process, as we discuss below [75].

The second effect that alters the bias field is the near field of the THz radiation. This process will be present for all types of emitters, since there will always be a near-field component of the radiated THz emission. This process has been observed and analyzed most extensively in the context of the large-aperture emitters with an in-plane bias field and in-plane current. For these devices, as just discussed, the space-charge effects will be of little importance, but radiative screening effects must be considered. In particular, if the radiated THz field has a component along the direction of the bias field, its ability to limit the output of the THz radiation is clear. This phenomenon has been observed and widely studied in large-aperture emitters excited by an ultrafast laser pulse at normal incidence, for which the near-field radiation is parallel, but opposite to the bias field.

To incorporate both of these effects into a model, we may write an effective bias field that carriers experience in the active area of a THz photoconductive

emitter as

$$\boldsymbol{E}_{\rm eff}(\boldsymbol{r},t) = \boldsymbol{E}_{\rm b}(\boldsymbol{r}) + \boldsymbol{E}_{\rm sc}(\boldsymbol{r},t) + \boldsymbol{E}_{\rm rad}(\boldsymbol{r},t)\,. \tag{32}$$

In this expression $\boldsymbol{E}_{\rm b}(\boldsymbol{r})$ denotes the static bias field, whether from a depletion field or an externally applied bias, and $\boldsymbol{E}_{\rm sc}(\boldsymbol{r},t)$ and $\boldsymbol{E}_{\rm rad}(\boldsymbol{r},t)$ denote, respectively, the space-charge field and the near-field value of the THz radiation. In our discussion, we first consider, in Sect. 6.1, the influence of space-charge screening on THz emission. This type of ultrafast field dynamics has also been found to be coupled with coherent modes in solids, which will be briefly examined in Sect. 6.2. In Sect. 6.3, we consider saturation effects caused by the near-field screening of the THz radiation.

6.1 Space-Charge Screening

To find the space-charge electric field, we need to consider the drift of the electrons and holes under the influence of the electric field and the resulting response of the electric field to this charge separation. Given the mutual interactions between the motion of the carriers and the electric fields, such modeling of transient behavior requires, even for the simplest model of the carrier dynamics, that one solves a system of coupled partial differential equations. In general, one needs to solve for the electric fields including retardation effects, that is, using the complete Maxwell's equations. For sufficiently small spatial dimensions (typically $\ll 1\,$mm for the usual duration of THz pulses) retardation may be neglected, and we can revert simply to a solution of the electrostatics problem. This is the situation that we now consider briefly. Because of its relative simplicity, we first present some results related to bias fields lying in the plane of the surface for which the initial bias field can be considered as spatially homogeneous. Our discussion follows the treatment of [76,77,78].

One component of this system of equations is comprised of continuity equations for electron and hole densities as a function of position and time. The essential spatial variation occurs along the direction of the bias field (which defines the y-axis) and only this spatial coordinate will be considered. In a simple case we can write continuity equations for electron density $n(y,t)$ and hole density $p(y,t)$ in the emitter as

$$\frac{\partial n,p(y,t)}{\partial t} = N(t,y) \pm \frac{1}{e}\frac{\partial j_{\rm n,p}(y,t)}{\partial y}\,. \tag{33}$$

Here $N(y,t)$ is the carrier injection rate (equal for electrons and holes) associated with excitation by the femtosecond laser pulse, and $j_{\rm n}$ and $j_{\rm p}$ are the electron and hole current densities. These current densities can be related to the effective bias field $\boldsymbol{E}_{\rm eff}(\boldsymbol{r},t) = \boldsymbol{E}_{\rm b}(\boldsymbol{r}) + \boldsymbol{E}_{\rm sc}(\boldsymbol{r},t)$ through a transport model such as that of (20). Here for clarity we have shown the continuity

equation, neglecting carrier recombination, trapping, and diffusion processes, which can be taken into account by modifying (33) [76,78].

The second component of the set of coupled differential equations is Poisson's equation for the electric field generated by the space charges,

$$\frac{\partial E_{\mathrm{sc}}(y,t)}{\partial y} = \frac{4\pi e}{\varepsilon}\left[n(y,t) - p(y,t)\right] . \tag{34}$$

As mentioned above, a more complete application of Maxwell's equations would be required if the relevant spatial dimensions are large enough to mandate to require consideration of retardation effects.

Iverson et al. [76] have solved these equations numerically for device structures with an in-plane bias field and differing bias and excitation conditions. Some results are illustrated in Fig. 15 for transient current or, equivalently, the shape of the near-field THz waveform, in a GaAs emitter with electrodes separated by 50 μm. The laser excitation is assumed to be of 100-fs duration and to have a Gaussian spatial profile also of 50-μm width. The results shown in the figure for the THz field have been smoothed by convoluting with a response function of a detector with a 1-ps response time. At low excitation densities, such as $1 \times 10^{15}\,\mathrm{cm}^{-3}$ shown in the top panel of the figure, the photocurrent rises rapidly as the laser excitation pulse injects carriers. The transient current then decreases slowly as carrier-trapping effects and recombination effects, which have been included in this analysis, gradually reduce the density of mobile carriers.

Results for higher carrier densities, associated with high pump laser fluence, are shown in the other panels of the figure. As the carrier densities are increased, the results reveal that peak transient currents (and, hence, THz fields) no longer scale proportionately, as they do at low carrier densities. At carrier densities of $1 \times 10^{17}\,\mathrm{cm}^{-3}$, for example, the peak THz field is approximately half as large as it would be in the absence of saturation effects. A more striking and characteristic aspect of the charge-screening process, however, is the change in shape of the current transient. When strong space-charge screening is present, the current transient develops a more sharply peaked structure. This arises because the onset of the space-charge field partially cancels the bias field, which in turn leads to a rapid decrease in the transient photocurrent. At an excitation density of $10^{17}\,\mathrm{cm}^{-3}$, the effect of space-charge screening is already visible at a few picoseconds after photoexcitation. As a function of the bias field, the influence of space-charge effects is more pronounced at higher biases, as one expects given the large induced photocurrents.

For typical experimental conditions where the THz radiation is measured in the far field, the change in shape of the photocurrent transient has a clear consequence. As we have discussed above in Sect. 3, the far-field THz waveform follows the time derivative of the current transient. Thus, at low excitation densities where the current density rises sharply and decays slowly, one will observe a nearly unipolar electric-field waveform. This shape arises

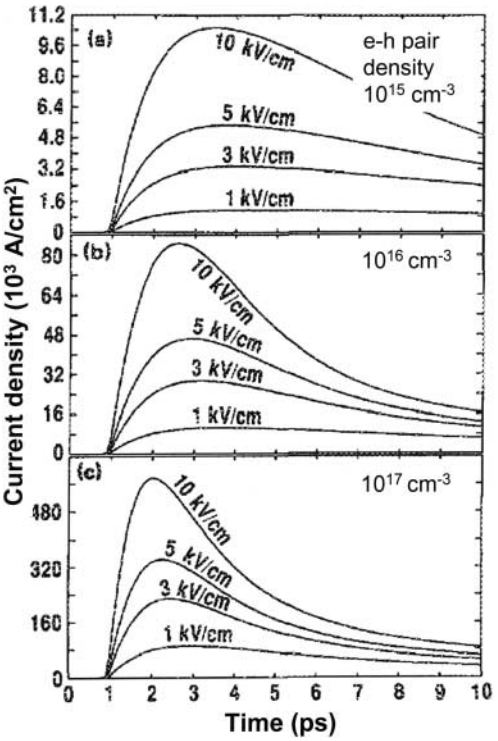

Fig. 15. Computed response by *Iverson* et al. [76] of a GaAs photoconductor with a 50-μm gap spacing and bias fields of 1, 3, 5, 10 kV/cm for three different carrier-excitation densities. As discussed in the text, the figure shows the influence of space-charge screening both through reduction in the expected value of the peak current and through the enhanced decay rate of the current transient associated with the screening of the bias field

from the rapidly rising edge of the current. The slow decay of the current density only produces a small (but persistent) negative tail in the waveform. At high excitation densities, on the other hand, the current density still rises rapidly, but also decays reasonably quickly. Thus, one observes a far-field THz electric-field waveform that appears to be bipolar. The general trend is that space-charge screening converts a more unipolar waveform to a bipolar shape.

For the case of in-plane current transients, the space-charge effects just considered diminish in importance, as we have argued, with increased lateral spatial dimensions. For large-area devices based on currents perpendicular to the surface this is not the case, and space-charge screening is generally the dominant limiting factor in efficiency of such devices. This is particularly true for devices using surface-depletion fields, which are inherently inhomogeneous on a very short length scale, typically of ~ 100 nm. The simulation of space-

charge screening in such geometries is conceptually similar to that described above, although different boundary conditions will generally be relevant at the surface compared to the interface with an electrode in the geometry with lateral current flow.

An example of space-charge screening for a depletion-field device, taken from the work of *Kersting* et al. [79], is displayed in Fig. 16. Here the authors have simulated the behavior of a GaAs surface with n-type doping ($1.7 \times 10^{16}\,\mathrm{cm}^{-3}$) under excitation by a 100-fs laser pulse. When the carrier-excitation density approaches the doping density of the sample, the charge distribution begins to be strongly altered. The figure shows the spatial variation of the electron and hole densities during (0 fs) and (500 fs) after excitation at a density of electron–hole pairs of $10^{16}\,\mathrm{cm}^{-3}$. A major redistribution of the charge density is seen to occur. This in turn gives rise to a significant change in the depletion field, the effective bias field in this problem. The figure shows the resulting spatial profile for a Schottky model of the surface with Fermi-level pinning at various times after photoexcitation. The assumed Fermi-level pining results in a constant field at the surface. The motion of the photoexcited carriers causes, however, the width of the depletion zone to decrease significantly.

6.2 Plasma Oscillations

The space-charge field discussed above arises from the separation of the photogenerated electrons and holes moving in the bias field and the development of regions of net positive and negative charge. Under appropriate circumstances, this perturbation can drive collective or plasma oscillations of the carriers. Such plasma oscillations initiated by ultrafast photoexcitation have been observed both in time-resolved photoreflectivity (photoabsorption) measurements [80,81,82] and in the THz emission measurements. In this section, we provide a brief description of the behavior of the latter.

The role of plasma oscillations in THz emission was first considered by *Jepsen* et al. [42] for a dipole emitter. Investigations of this phenomenon in large-area emitters, both with and without external magnetic fields, were subsequently pursued by several groups [67,68,74,79,83]. THz emission has been observed experimentally from coherent 3D plasma excitations formed both from photogenerated carriers in the intrinsic zone of GaAs p–i–n diodes [68,83] and from extrinsic carriers in n-doped GaAs [79]. In the latter case, the plasma oscillation of the extrinsic carriers is believed to be initiated by the ultrafast dynamics of the surface-depletion field. This coupling arises because the extrinsic electrons are confined between the undoped substrate of the structure and the surface-depletion region. Photoexcitation of the material causes an impulsive change of the depletion field, which then drives the plasma oscillation of the cold electrons.

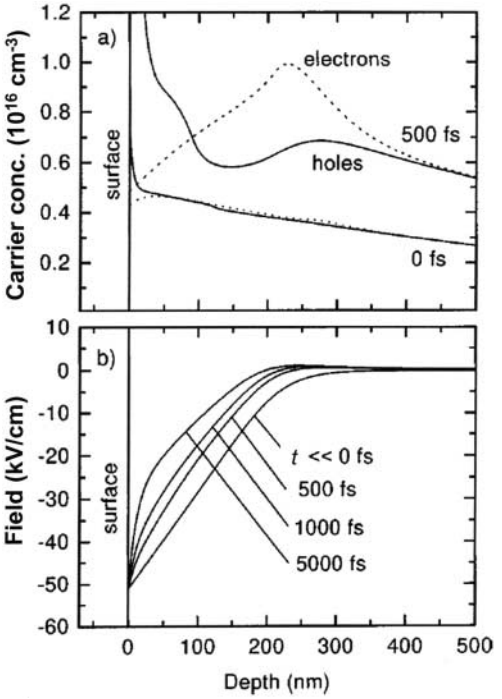

Fig. 16. Calculated response, after *Kersting* et al., to photoexcitation of surface region of a model GaAs sample: (**a**) Densities of photogenerated electrons (*dashed lines*) and holes (*solid lines*) at the surface of an n-doped (1.7×10^{16} cm^{-3}) GaAs sample during excitation (0 fs) and 500 fs after excitation. The excitation density of electron–hole pairs is taken to be 10^{16} cm^{-3}. (**b**) The surface depletion field before and at various times after photoexcitation. The changes are the result of space-charge screening. (After [79])

6.2.1 Drude Model with Plasma Oscillations

Since the Drude–Lorentz model has provided an adequate qualitative explanation for the behavior of THz emitters at low excitation densities, it is appropriate also to consider plasma oscillations within this framework. For this purpose, it is convenient to introduce a space-charge polarization $\boldsymbol{P}_{\rm sc}(\boldsymbol{r},t)$ to describe the charge separation associated with the motion of the electron–hole pairs. In this language, the charge-continuity equation takes the form:

$$\frac{\partial \boldsymbol{P}_{\rm sc}(\boldsymbol{r},t)}{\partial t} = -\frac{\boldsymbol{P}_{\rm sc}(\boldsymbol{r},t)}{\tau_{\rm c}} + \boldsymbol{j}(\boldsymbol{r},t)\,, \tag{35}$$

where $\boldsymbol{j}(\boldsymbol{r},t)$ is the total photocurrent density and $\tau_{\rm c}$ denotes the lifetime of mobile carriers. In undamaged materials, since $\tau_{\rm c}$ usually far exceeds the relevant time scale of (35) we therefore assume the carrier density to be time

independent during the period of time relevant for THz emission and neglect the first term in (35). If we further neglect the contribution of the holes, which generally have considerably lower mobility than the electrons, we can write $\boldsymbol{P}_{\rm sc}(\boldsymbol{r},t) \approx -en(\boldsymbol{r})\boldsymbol{\xi}$, where $n(\boldsymbol{r})$ is the electron density and $\boldsymbol{\xi}$ denotes the local displacement of electrons under the influence of the effective bias field.

This induced polarization modifies the initial bias field $\boldsymbol{E}_{\rm b}(\boldsymbol{r})$ to produce the time-dependent effective bias field $\boldsymbol{E}_{\rm eff}(\boldsymbol{r},t)$ according to

$$\boldsymbol{E}_{\rm eff}(\boldsymbol{r},t) = \boldsymbol{E}_{\rm b}(\boldsymbol{r}) + 4\pi\boldsymbol{P}_{\rm sc}(\boldsymbol{r},t)/\eta\varepsilon \approx \boldsymbol{E}_{\rm b}(\boldsymbol{r}) - (4\pi e/\eta\varepsilon)n(\boldsymbol{r})\boldsymbol{\xi}\,. \tag{36}$$

Here, η is a dimensionless phenomenological geometric factor for screening, with $\eta \approx 1$ for a thin polarization sheet. Let us now consider the case where the carrier density is approximately spatially uniform, $\eta(\boldsymbol{r}) = \eta$. We can then combine (36) with the Drude model to describe the motion of carriers under the effective bias field to obtain

$$\frac{d^2\boldsymbol{\xi}}{{\rm d}t^2} + \frac{1}{\tau}\frac{d\boldsymbol{\xi}}{{\rm d}t} + \omega_{\rm p}^2\boldsymbol{\xi} = \frac{e}{m^*}\boldsymbol{E}_{\rm b}\,. \tag{37}$$

Here, $\omega_{\rm p} = \sqrt{4\pi ne^2/m^*\varepsilon}$ is the plasma frequency, and τ is the carrier-scattering time for momentum changing collisions, as discussed above in Sect. 3.

Equation (37) is simply that of a damped harmonic oscillator. Its solution can be readily found for the appropriate initial conditions of $\boldsymbol{\xi}(t=0) = 0$ and $\boldsymbol{v}(t=0) = 0$ as

$$\boldsymbol{v}(t) = \frac{e}{m^*\omega}\boldsymbol{E}_{\rm b}{\rm e}^{-(2/\tau)t}\sin\omega t\,, \tag{38}$$

with an oscillation frequency of

$$\omega = \sqrt{\omega_{\rm p}^2 - (1/2\tau)^2}\,. \tag{39}$$

Depending on the values of $\omega_{\rm p}\tau/2$, three types of behavior may emerge: underdamping ($\omega_{\rm p}\tau/2 > 1$), critical damping ($\omega_{\rm p}\tau/2 = 1$), and overdamping ($\omega_{\rm p}\tau/2 < 1$). The corresponding three types of response are illustrated in Fig. 17. Oscillatory features appear only in the underdamped limit of $\omega_{\rm p}\tau/2 > 1$. In this case, the carrier velocity (or, equivalently, current density or near-field THz radiation) oscillates with a frequency ω and a damping rate of $2/\tau$.

Now let us return to the important question of when such plasma oscillations become important in THz emitters. The system has to fulfill several requirements. First, the photoexcitation has to be fairly spatially uniform so that the charge carriers oscillate at the same frequency and add coherently. In many GaAs p–i–n diodes and n-doped structures, this condition can be satisfied, since the absorption depth of the material is much greater than the thickness of the active region of the emitter. Secondly, the carriers have to

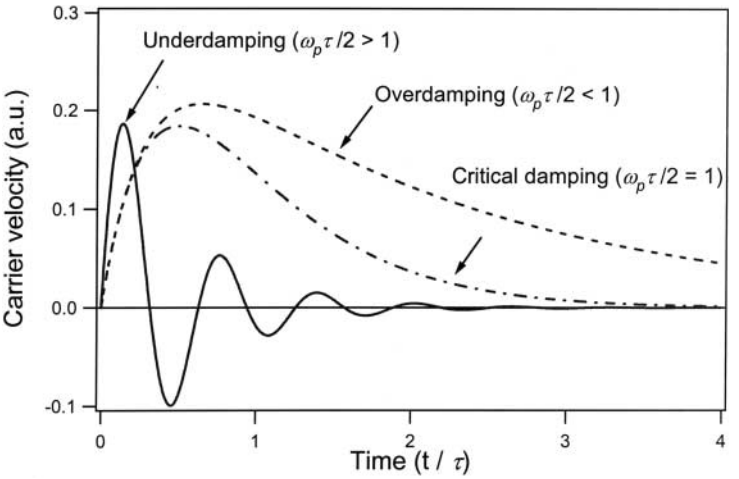

Fig. 17. Illustration of three different regimes of damping for plasma oscillations

start oscillating in phase. This criterion can be met if the optical excitation pulse is much shorter in duration than the period of the plasma oscillations. Finally, to ensure that we are in the underdamped regime of oscillation, the scattering time of the electrons must be long enough so that $\omega_{\mathrm{p}}\tau/2 > 1$. In a real system such as GaAs, for instance, the (bulk) electron scattering time is $\sim 350\,\mathrm{fs}$ at room temperature. Thus, to be in the underdamped regime, we need a plasma frequency of the carriers larger than $\sim 1\,\mathrm{THz}$. This would require an achievable carrier density of $\sim 10^{16}\,\mathrm{cm}^{-3}$. The impulsive excitation criterion would also be satisfied for a typical laser excitation pulse of approximately 100 fs duration. Obviously, plasma oscillations will be still easier to observe at low temperatures where the carrier-scattering times are significantly longer and $\omega_{\mathrm{p}}\tau/2 \gg 1$ can be satisfied.

6.2.2 Experimental Observations of Plasma Oscillations

In this section, we describe some of the experimental studies of THz generation that exemplify the role that plasma oscillations can play. The first example, from the investigations of *Andrews* et al. [68], concerns THz emission by excitation of the carriers in the intrinsic region of a GaAs p–i–n diode comprised of a 200-nm *n*-doped layer, a 500-nm intrinsic layer, and a 200-nm *p*-doped layer. Data for the THz electric field are shown in Fig. 18a for a sample temperature of 10 K. Evidence of plasma oscillations is clear in the THz waveforms. The THz electric field does not precisely follow the simple exponentially damped form because inhomogeneity in the excitation density produces a distribution of plasma frequencies. The oscillation frequency of the THz transients was extracted by Fourier transformation of the time-domain waveforms. Figure 18b shows that this frequency varies with the square

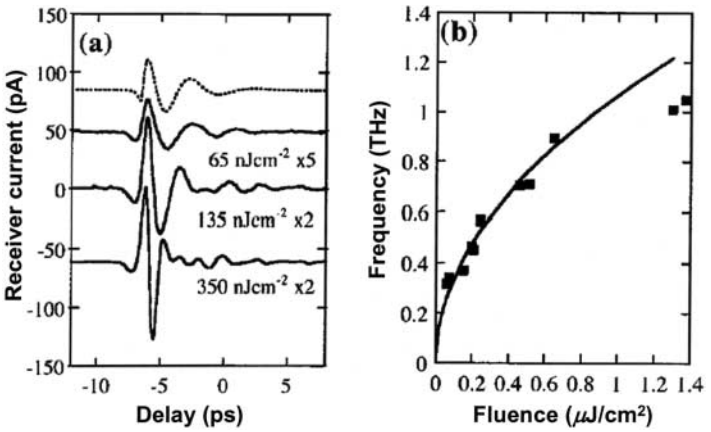

Fig. 18. (**a**) THz electric field emitted from a GaAs p–i–n diode at 10 K. The *dotted curve* is the simulated waveform within the Drude model for a fluence of 65 nJ/cm^2. (**b**) Variation of mean plasma frequency with pump fluence. The *solid curve* is a square-root variation as expected for a plasma oscillation of the photogenerated carriers. (After results of *Andrews* et al. [68])

root of the laser excitation fluence. This is just the behavior expected for a plasma oscillation in which the frequency scales with the square root of the carrier density $\omega = \sqrt{\omega_\mathrm{p}^2 - 1/4\tau^2} \approx \omega_\mathrm{p} \propto \sqrt{n}$ and hence with the square root of the excitation fluence (in the intrinsic region of the p–i–n structure). The dashed line in Fig. 18a represents the result of simulation based on the Drude model for carrier dynamics for an excitation fluence of 65 nJ/cm^2. The good agreement between the simulation and experiment here is another example of successful application of this model.

A related, but distinct phenomenon can be observed in semiconductor structures with static densities of carriers, so-called cold electrons, provided by doping. Figure 19 shows results of *Kersting* et al. [79] for two GaAs samples with different levels of n-type doping. In these measurements the center frequency of the THz emission is plotted as a function of excitation density. In contrast to the case just discussed, here we see no significant change in the plasma frequency over the indicated range of excitation densities. On the other hand, this frequency does change with doping concentration. These results strongly support the notion that the observed plasma oscillation is associated with motion of the extrinsic electrons in the bulk, rather than the response of the photogenerated carriers.

6.3 Near-Field Screening in Large Emitters

Both space-charge screening and near-field radiation screening may alter the bias field of a THz emitter and thus strongly affect its output. In large-area

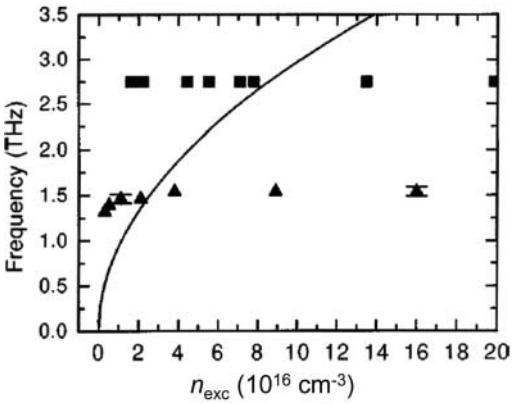

Fig. 19. Dependence of the THz emission frequency on excitation density in *n*-doped GaAs. The *triangles* and *squares* show data recorded for structures with doping concentration of 1.7×10^{16} and 1.1×10^{17} cm^{-3}, respectively. The *solid line* shows the dependence of the frequency for a photoexcited electron plasma that would be expected according to (39). (After results of *Kersting* et al. [79])

THz emitters in which the current flows in the plane of the surface, space-charge screening is, as discussed in Sect. 6.1, relatively minor for emitters with lateral dimensions of ~ 1 mm or more. This can be understood as a consequence of the retardation time needed for the effect of charge separation at the boundary of the material to be felt elsewhere. Therefore, large-aperture emitters are particularly well suited for the study of the near-field screening effects in which the transient current is modified by the THz field that it generates.

Saturation effects in large-aperture emitters were first reported by *Darrow* et al. [47,48] and were subsequently the subject of many additional experimental investigations [46,49,77]. A typical result of the saturation characteristics of such a structure is shown as Fig. 8 in Sect. 4. As this figure illustrates, the strength of the emitted THz field no longer grows linearly with increasing fluence as it does in the low fluence limit, but rather reaches a saturated level. The value of this saturated THz field strength is seen to scale roughly in proportion to the strength of the dc bias field.

The basic characteristics of this saturation effect can be understood quite satisfactorily within the context of a simple model of near-field screening first introduced by *Darrow* et al. [47] and examined in considerable depth subsequently by other researchers [37,46,49,84,85]. The principle is identical to that discussed above for space-charge screening, namely, that the carriers do not move simply in the initial applied bias field, but rather in an effective bias field resulting from the modification of the original bias field caused by the photoinduced charge carriers. In this case, the key aspect of the charge carriers is the current that they generate and the radiation field associated

with it. The analyses performed to date have all introduced a significant simplification that permits a closed-form analytical result to be obtained. It is the assumption that the carriers respond instantaneously to the applied bias field, that is, that they immediately move at the steady-state velocity defined by an appropriate carrier mobility. This can be considered as the limit of the Drude–Lorentz model when the scattering rate is taken to be much shorter than the other characteristic time scale in the problem, namely the laser pulse duration. It neglects the transient mobility that has been seen to be important in describing other aspects of THz emission from photoconductors excited by ultrafast laser pulses. While the accuracy of this approximation for laser pulses of a duration of the order of 100 fs is questionable, this simplification has great merits in permitting a ready analysis of the phenomenon. The results of this treatment yield the qualitative features seen experimentally. Quantitative agreement should not be expected as a rule, but would be approached in materials with high scattering rates (perhaps enhanced by carrier–carrier scattering present at high excitation densities) or for excitation by relatively long laser pulses. It should be noted that in addition to the interest of this topic for modeling the properties of high-power THz emitters, the problem also allows one to examine carrier transport in certain extreme regimes, such as that of high carrier density and/or high bias-field strength. Here we first review this theory of saturation by near-field screening and then provide some comparison with experimental findings.

Within the approximation of an instantaneous carrier response to the effective bias field, the relation between the current density and the bias field is simply

$$\boldsymbol{j}(t) = e\overleftrightarrow{\boldsymbol{\mu}}_{\mathrm{dc}} N(t) \boldsymbol{E}_{\mathrm{eff}}(t)\,. \tag{40}$$

Such a linear relation between the current density and bias field is sometimes termed an "Ohm's law" response. For simplicity, we have dropped the spatial dependence in (40), which is not essential for the current discussion. The effective bias field in (40) is the sum of the static bias field and the electric field of the THz radiation evaluated in the near field:

$$\boldsymbol{E}_{\mathrm{eff}}(t) = \boldsymbol{E}_{\mathrm{b}} + \boldsymbol{E}_{\mathrm{rad}}(t)\,. \tag{41}$$

Combing these two equations with the expression for the near-field THz radiation (6), we obtain for THz radiation in the near field from a large-aperture emitter

$$E_{\mathrm{rad}}(t) = -E_{\mathrm{b}} \frac{\frac{4\pi}{c}\sigma_{\mathrm{s}}(t)}{\frac{4\pi}{c}\sigma_{\mathrm{s}}(t) + (1+\sqrt{\varepsilon})}\,. \tag{42}$$

Here we assume normal incidence for the laser excitation and that the bias field $\boldsymbol{E}_{\mathrm{b}}$ lies in the plane of the surface, as appropriate for the large-aperture emitter. The surface conductivity has been introduced as $\overleftrightarrow{\boldsymbol{\sigma}}_{\mathrm{s}}(t) = de\overleftrightarrow{\boldsymbol{\mu}}_{\mathrm{dc}} N(t)$,

where d is the effective thickness of the surface layer in which photocurrent exists. In materials with isotropic mobilities, as shown in (42), the radiated field is directed parallel, but opposite to the bias field. This is the origin of the screening effect.

Let us examine some of the properties contained in (42). First let us consider the limiting behaviors. The simple unscreened or unsaturated result emerges when the fluence is sufficiently low so that $\sigma_s \ll (1+\sqrt{\varepsilon})\, c/4\pi$. In this case, the radiated field scales with surface conductivity or, equivalently, with the laser fluence, as expected. On the other hand, for a sufficiently high excitation density (or surface conductivity), the near-field THz emission approaches a peak value of $-E_b$. When this condition is reached, the bias field will be fully screened and $\boldsymbol{E}_{\text{eff}}(t) = \boldsymbol{E}_b + \boldsymbol{E}_{\text{rad}}(t)$ will approach zero. As expected, this limit does not depend on any material transport properties nor on any of the details of the shape of the laser excitation pulse. The saturation value of the radiated field does scale, however, directly with the strength of the applied bias field.

Between these two limits, the onset of saturation occurs when the surface conductivity approaches $\sigma_s(t) = (1+\sqrt{\varepsilon})\, c/4\pi$. Analysis of the saturation curve then permits one to determine the experimental surface conductivity where saturation begins. Since the corresponding laser fluence can be converted into a surface carrier density by considering the amount of absorbed energy, knowledge of the sheet conductivity permits one to infer the effective carrier mobility. In the simplest implementation of these models, the mobility is just treated as a constant to represent an averaged value relevant over the course of the THz emission process. Hot-carrier effects and carrier–carrier scattering may also be incorporated within this model by introducing a phenomenological carrier mobility that depends on the elapsed time since photogeneration of the carriers and on the carrier density [37].

The radiation in the far field behaves similarly to that in the near field with respect to saturation. The far-field solution can be determined from the near-field solution by computing its first time derivative. To make a direct comparison with experimental observations (Figs. 7 and 8), *Benicewicz* and *Taylor* [46] have considered the relevant experimental details for the actual case of a spatially inhomogeneous pump beam and a far-field THz detector having a finite response time τ_d. These authors considered the behavior in the limit that the carrier lifetime $\tau_c \gg$ response time of the detector $\tau_d \gg$ laser pulse duration. They predict that the peak of the radiated THz electric field in the far field varies as a function of the excitation fluence F according to the relation:

$$E_{\text{rad,peak}} \approx -DE_b \frac{F/F_0}{1+F/F_0}\,. \tag{43}$$

Here the constant D is a measure of the fraction of the bias field detected in the far field; F_0 is the saturation excitation fluence, defined as the optical fluence necessary to generate half of the maximum THz field.

Comparison of the predicted peak radiation in the far field (solid lines) with experiment (symbols) is shown in Figs. 7 and 8 in Sect. 4. The dependence of the peak radiation in the far field on the bias fields up to 12 kV/cm and on the excitation fluence up to 1 mJ/cm^2 has been studied for several large-aperture emitters based on InP and GaAs photoconductors photoconductor. The predicted linear dependence of the radiation peak on the bias field has been verified for a large range of excitation fluences. The saturation characteristics are found to be compatible with the form of (43). The inferred saturation fluence, F_0, is related to the peak sheet conductivity. Hence, as discussed above, it can be used to determine the effective carrier mobility (where the sheet carrier density is determined by the laser fluence). A value of $430 \pm 100\,\mathrm{cm}^2/\mathrm{V} \cdot \mathrm{s}$ was inferred for GaAs [46]. This value is considerably lower than the steady-state (room-temperature) mobility of $4600\,\mathrm{cm}^2/\mathrm{V} \cdot \mathrm{s}$ for bulk GaAs. This discrepancy was attributed to hot-electron effects and carrier–carrier scattering [46].

The simple model of instantaneous carrier response predicts the correct dependence of the radiation on the bias field and the correct form of the saturation of the THz emission with increasing excitation fluence. The inferred values for mobilities, however, differ significantly from the usual steady-state properties of the bulk materials. While this difference may be the consequence of hot-carrier effects or carrier–carrier interactions, as suggested in previous investigations, it may also reflect the inherent inaccuracy of a model that relies on the assumption of an instantaneous carrier response. The severity of approximation is apparent when one notes that the typical duration of excitation pulses of 100 fs is actually shorter than carrier scattering times in many semiconductors. A more realistic model for carrier transport is therefore probably required to obtain better quantitative agreement in most material systems.

Another factor of practical importance for high-power THz emitters is worth mentioning here. Saturation effects are seen in large-aperture emitters at laser fluence substantially below 1 mJ/cm^2 (Fig. 8). These values lie below fluences that can be achieved by common ultrafast laser sources, as well as below the optical damage thresholds of common photoconductive media. Thus, possible methods for circumventing these saturation effects are desirable in order to exploit most effectively the capabilities of current femtosecond-laser systems for the generation of intense THz radiation. In this regard, we should note the possibility of the generation of narrowband THz radiation. Such narrowband (or otherwise spectrally structured) THz radiation can be produced using appropriately shaped optical excitation pulses, such as obtained from the chirped pulse-mixing scheme of *Weling* et al. [85,86,87] or from optical pulse-shaping techniques [88,89]. These schemes permit one to use temporally longer optical excitation pulses that have been optimized to produce THz radiation in the desired spectral range. The increased temporal duration of the pulses, when appropriately shaped, does not diminish

the amount of THz emission in the desired spectral range. It does, however, alleviate saturation effects in photoconductive materials with relatively short carrier lifetimes. The improvement in the saturation characteristics [85,89] is the result of a reduction in the peak photoinduced surface conductivity when a given laser excitation fluence is applied over a longer period of time.

7 Conclusions

In this chapter, we have attempted to give an overview of the current state in the generation of THz radiation using photoconductive emitters with femtosecond laser excitation. The discussion has centered on large-area structures. These structures have the merits of simplicity and scalability to high powers. In the context of this chapter, however, they are especially attractive because of the relative simplicity of their radiation mechanism. In addition, there exists an extensive literature describing the properties of such emitters, including the influence of material properties, magnetic fields, and saturation phenomena. Our discussion has included both structures with bias fields in the plane of the surface and perpendicular to it. These fields may be externally applied, for the in-plane case, or may originate from built-in fields. In either case, the fundamentals of the emission process are rather similar, although the exact waveforms and saturation mechanisms naturally reflect the particular configuration under consideration.

While considerable progress has been made in developing such THz emitters, as the discussion in this chapter may serve to illustrate, the possibility for further improvements is clear. For example, the notion of more efficient THz emission from transient currents flowing perpendicular to the surface plane through the use of prisms, a scheme that resulted from consideration of the mechanism involved in magnetic-field enhancements, was only recently demonstrated [73]. Further, such large-area photoconductive THz emitters combined with current femtosecond modelocked lasers and, perhaps, electro-optic sampling techniques to achieve maximal detection bandwidth [90,91,92,93,94], provide many opportunities for the investigation of ultrafast carrier dynamics in a variety of materials. These experiments may be regarded as THz emission measurements for characterization of carrier-transport properties [38,57,75,95,96,97,98]. Although some noteworthy experiments have already been carried out illustrating these concepts, much further progress can be anticipated. By the same token, the high-power THz pulses produced by such emitters also offer novel possibilities for spectroscopic studies. The most striking possibility would be measurements in which the intense THz pulses serve not to probe materials, but to induce changes in them [99,100,101,102]. Such measurements are clearly challenging and still remain in their infancy. They do, however, hold many interesting possibilities as a new means of investigating material response to ultrafast perturbations.

Acknowledgements

One of the authors (TFH) acknowledges primary support for this work by the Nanoscale Science and Engineering Initiative of the National Science Foundation under NSF Award CHE-0117752.

References

1. D. H. Auston: Ultrafast optoelectronics, in W. Kaiser (Ed.): *Ultrashort Laser Pulses* (Springer, Berlin, Heidelberg 1993) 1
2. D. R. Grischkowsky: Nonlinear generation of sub-psec pulses of THz electromagnetic radiation by optoelectronics – Application to time-domain spectroscopy, in H. Walther, N. Koroteev, M. O. Scully (Eds.): *Frontiers in Nonlinear Optics* (Institute of Physics, Philadelphia 1993) 1, 2, 12, 13, 15, 20
3. W. M. Robertson: *Optoelectronic Techniques for Microwave and Millimeter-Wave Engineering* (Artech House, Boston 1995) 1
4. G. Mourou, C. V. Stancampiano, A. Antonetti, A. Orszag: Picosecond microwave pulses generated with a subpicosecond laser-driven semiconductor switch, Appl. Phys. Lett. **39**, 295 (1981) 1
5. G. Mourou, C. V. Stancampiano, D. Blumenthal: Picosecond microwave pulse generation, Appl. Phys. Lett. **38**, 470 (1981) 1
6. R. Heidemann, T. Pfeiffer, D. Jager: Optoelectronically pulsed slot-line antennas, Electron. Lett. **19**, 316 (1983) 1
7. A. P. Defonzo, C. R. Lutz: Optoelectronic transmission and reception of ultrashort electrical pulses, Appl. Phys. Lett. **51**, 212 (1987) 1
8. W. M. Robertson, G. Arjavalingam, S. L. Shinde: Microwave dielectric measurements of zirconia-alumina ceramic composites – A test of the Clausius–Mossotti mixture equations, J. Appl. Phys. **70**, 7648 (1991) 2
9. H. Harde, J. Zhao, M. Wolff, R. A. Cheville, D. Grischkowsky: THz time-domain spectroscopy on ammonia, J. Phys. Chem. A **105**, 6038 (2001) 2
10. T. I. Jeon, D. Grischkowsky, A. K. Mukherjee, R. Menon: Electrical characterization of conducting polypyrrole by THz time-domain spectroscopy, Appl. Phys. Lett. **77**, 2452 (2000) 2
11. G. Gallot, J. Q. Zhang, R. W. McGowan, T. I. Jeon, D. Grischkowsky: Measurements of the THz absorption and dispersion of ZnTe and their relevance to the electro-optic detection of THz radiation, Appl. Phys. Lett. **74**, 3450 (1999) 2
12. R. A. Cheville, D. Grischkowsky: Far-infrared foreign and self-broadened rotational linewidths of high-temperature water vapor, J. Opt. Soc. Am. B **16**, 317 (1999) 2
13. T. I. Jeon, D. Grischkowsky: Characterization of optically dense, doped semiconductors by reflection THz time-domain spectroscopy, Appl. Phys. Lett. **72**, 3032 (1998) 2
14. H. Harde, R. A. Cheville, D. Grischkowsky: Terahertz studies of collision-broadened rotational lines, J. Phys. Chem. A **101**, 3646 (1997) 2
15. R. A. Cheville, D. Grischkowsky: Far-infrared terahertz time-domain spectroscopy of flames, Opt. Lett. **20**, 1646 (1995) 2

16. S. E. Ralph, S. Perkowitz, N. Katzenellenbogen, D. Grischkowsky: Terahertz spectroscopy of optically thick multilayered semiconductor structures, J. Opt. Soc. Am. B **11**, 2528 (1994) 2
17. C. Ronne, L. Thrane, P. O. Astrand, A. Wallqvist, K. V. Mikkelsen, S. R. Keiding: Investigation of the temperature dependence of dielectric relaxation in liquid water by THz reflection spectroscopy and molecular dynamics simulation, J. Chem. Phys. **107**, 5319 (1997) 2
18. C. Ronne, P. O. Astrand, S. R. Keiding: THz spectroscopy of liquid H_2O and D_2O, Phys. Rev. Lett. **82**, 2888 (1999) 2
19. M. Schall, H. Helm, S. R. Keiding: Far infrared properties of electro-optic crystals measured by THz time-domain spectroscopy, Int. J. Infrared Millimeter Waves **20**, 595 (1999) 2
20. P. G. Huggard, J. A. Cluff, G. P. Moore, C. J. Shaw, S. R. Andrews, S. R. Keiding, E. H. Linfield, D. A. Ritchie: Drude conductivity of highly doped GaAs at terahertz frequencies, J. Appl. Phys. **87**, 2382 (2000) 2
21. H. G. Roskos, M. C. Nuss, J. Shah, B. Tell, J. Cunningham: Terahertz absorption between split subbands in coupled quantum wells, in T. C. L. G. Sollner, J. Shahand (Eds.): *Picosecond Electronics and Optoelectronics* (Opt. Soc. Am., Washington, DC 1991), Vol. 4 2
22. W. M. Robertson, G. Arjavalingam, R. D. Meade, K. D. Brommer, A. M. Rappe, J. D. Joannopoulos: Measurement of photonic band-structure in a 2-dimensional periodic dielectric array, Phys. Rev. Lett. **68**, 2023 (1992) 2
23. E. Ozbay, E. Michel, G. Tuttle, R. Biswas, K. M. Ho, J. Bostak, D. M. Bloom: Teraherz spectroscopy of 3-dimensional photonic band-gap crystals, Opt. Lett. **19**, 1155 (1994) 2
24. M. C. Nuss, K. W. Goossen, J. P. Gordon, P. M. Mankiewich, M. L. Omalley, M. Bhushan: Terahertz time-domain measurement of the conductivity and superconducting band-gap in niobium, J. Appl. Phys. **70**, 2238 (1991) 2
25. R. A. Kaindl, M. A. Carnahan, J. Orenstein, D. S. Chemla, H. M. Christen, H. Y. Zhai, M. Paranthaman, D. H. Lowndes: Far-infrared optical conductivity gap in superconducting MgB_2 films, Phys. Rev. Lett. **88**, 027003 (2002) 2
26. J. S. Dodge, C. P. Weber, J. Corson, J. Orenstein, Z. Schlesinger, J. W. Reiner, M. R. Beasley: Low-frequency crossover of the fractional power-law conductivity in $SrRuO_3$, Phys. Rev. Lett. **85**, 4932 (2000) 2
27. J. Corson, J. Orenstein, S. Oh, J. O'Donnell, J. N. Eckstein: Nodal quasiparticle lifetime in the superconducting state of $Bi_2Sr_2CaCu_2O_{8+\delta}$, Phys. Rev. Lett. **85**, 2569 (2000) 2
28. A. G. Markelz, A. Roitberg, E. J. Heilweil: Pulsed terahertz spectroscopy of DNA, bovine serum albumin and collagen between 0.1 and 2.0 THz, Chem. Phys. Lett. **320**, 42 (2000) 2
29. J. T. Darrow, B. B. Hu, X. C. Zhang, D. H. Auston: Subpicosecond electromagnetic pulses from large-aperture photoconducting antennas, Opt. Lett. **15**, 323 (1990) 2, 20
30. X. C. Zhang, B. B. Hu, J. T. Darrow, D. H. Auston: Generation of femtosecond electromagnetic pulses from semiconductor surfaces, Appl. Phys. Lett. **56**, 1011 (1990) 2, 19, 20, 21
31. L. Xu, X. C. Zhang, D. H. Auston, B. Jalali: Terahertz radiation from large-aperture Si p–i–n diodes, Appl. Phys. Lett. **59**, 3357 (1991) 2

32. D. You, R. R. Jones, P. H. Bucksbaum, D. R. Dykaar: Generation of high-power sub-single-cycle 500-fs electromagnetic pulses, Opt. Lett. **18**, 290 (1993) 2
33. B. B. Hu, J. T. Darrow, X. C. Zhang, D. H. Auston, P. R. Smith: Optically steerable photoconducting antennas, Appl. Phys. Lett. **56**, 886 (1990) 2, 19
34. B. I. Greene, P. N. Saeta, D. R. Dykaar, S. Schmittrink, S. L. Chuang: Far-infrared light generation at semiconductor surfaces and its spectroscopic applications, IEEE J. Quantum Electron. **28**, 2302 (1992) 2, 21, 22
35. T. F. Heinz: Second-order nonlinear optical effects at surfaces and interfaces, in H.-E. Ponath, G. I. Stegeman (Eds.): *Nonlinear Surface Electromagnetic Phenomena* (North Holland, Amsterdam 1991) p. 353 6
36. J. Shan, C. Weiss, R. Wallenstein, R. Beigang, T. F. Heinz: Origin of magnetic field enhancement in the generation of terahertz radiation from semiconductor surfaces, Opt. Lett. **26**, 849 (2001) 7, 15, 27, 28, 29, 31, 33
37. A. J. Taylor, P. K. Benicewicz, S. M. Young: Modeling of femtosecond electromagnetic pulses from large-aperture photoconductors, Opt. Lett. **18**, 1340 (1993) 14, 23, 46, 48
38. B. B. Hu, E. A. Desouza, W. H. Knox, J. E. Cunningham, M. C. Nuss, A. V. Kuznetsov, S. L. Chuang: Identifying the distinct phases of carrier transport in semiconductors with 10-fs resolution, Phys. Rev. Lett. **74**, 1689 (1995) 14, 50
39. H. Roskos, M. C. Nuss, K. W. Goossen, D. W. Kisker, A. E. White, K. T. Short, D. C. Jacobson, J. M. Poate: Propagation of picosecond electrical pulses on a silicon-based microstrip line with buried cobalt silicide ground plane, Appl. Phys. Lett. **58**, 2604 (1991) 15, 27
40. P. C. M. Planken, M. C. Nuss, W. H. Knox, D. A. B. Miller, K. W. Goossen: THz pulses from the creation of polarized electron–hole pairs in biased quantum-wells, Appl. Phys. Lett. **61**, 2009 (1992) 15, 27
41. C. Waschke, H. G. Roskos, R. Schwedler, K. Leo, H. Kurz, K. Kohler: Coherent submillimeter-wave emission from Bloch oscillations in a semiconductor Superlattice, Phys. Rev. Lett. **70**, 3319 (1993) 15, 27
42. P. Uhd Jepsen, R. H. Jacobsen, S. R. Keiding: Generation and detection of terahertz pulses from biased semiconductor antennas, J. Opt. Soc. Am. B **13**, 2424 (1996) 15, 41
43. X. C. Zhang, D. H. Auston: Generation of steerable submillimeter waves from semiconductor surfaces by spatial light modulators, Appl. Phys. Lett. **59**, 768 (1991) 20
44. N. Froberg, M. Mack, B. B. Hu, X. C. Zhang, D. H. Auston, 500 GHz electrically steerable photoconducting antenna-array, Appl. Phys. Lett. **58**, 446 (1991) 20
45. P. Kuzel, M. A. Khazan, J. Kroupa: Spatiotemporal transformations of ultrashort terahertz pulses, J. Opt. Soc. Am. B **16**, 1795 (1999) 22
46. P. K. Benicewicz, A. J. Taylor: Scaling of terahertz radiation from large-aperture biased InP photoconductors, Opt. Lett. **18**, 1332 (1993) 23, 24, 25, 46, 48, 49
47. J. T. Darrow, X. C. Zhang, J. D. Morse: Saturation properties of large-aperture photoconducting antennas, IEEE J. Quantum Electron. **28**, 1607 (1992) 23, 46
48. J. T. Darrow, X. C. Zhang, D. H. Auston: Power scaling of large-aperture photoconducting antennas, Appl. Phys. Lett. **58**, 25 (1991) 23, 46

49. P. K. Benicewicz, J. P. Roberts, A. J. Taylor: Scaling of terahertz radiation from large-aperture biased photoconductors, J. Opt. Soc. Am. B **11**, 2533 (1994) 23, 46
50. P. N. Saeta, B. I. Greene, S. L. Chuang: Short terahertz pulses from semiconductor surfaces – The importance of bulk difference-frequency mixing, Appl. Phys. Lett. **63**, 3482 (1993) 25, 26
51. Y. R. Shen: *The Principles of Nonlinear Optics* (Wiley, New York 1984) 26
52. Y. R. Shen: *Nonlinear Infrared Generation* (Springer, Berlin, Heidelberg 1977) 26
53. A. Nahata, A. S. Weling, T. F. Heinz: A wideband coherent terahertz spectroscopy system using optical rectification and electro-optic sampling, Appl. Phys. Lett. **69**, 2321 (1996) 26
54. B. B. Hu, X. C. Zhang, D. H. Auston: Terahertz radiation induced by subband-gap femtosecond optical excitation of GaAs, Phys. Rev. Lett. **67**, 2709 (1991) 26
55. Y. Yafet, E. Yablonovitch: Virtual photoconductivity due to intense optical radiation transmitted through a semiconductor, Phys. Rev. B **43**, 12480 (1991) 26
56. A. V. Kuznetsov, C. J. Stanton: Ultrafast optical generation of carriers in a dc electric-field – Transient localization and photocurrent, Phys. Rev. B **48**, 10828 (1993) 26
57. B. B. Hu, A. S. Weling, D. H. Auston, A. V. Kuznetsov, C. J. Stanton: DC-electric-field dependence of THz radiation-induced by femtosecond optical excitation of bulk GaAs, Phys. Rev. B **49**, 2234 (1994) 26, 50
58. X. C. Zhang, Y. Jin, T. D. Hewitt, T. Sangsiri, L. E. Kingsley, M. Weiner: Magnetic switching of THz beams, Appl. Phys. Lett. **62**, 2003 (1993) 27, 28, 29
59. X. C. Zhang, Y. Jin: Influence of electric and magnetic fields on THz radiation, Appl. Phys. Lett. **62**, 2477 (1993) 27, 29
60. N. Sarukura, H. Ohtake, S. Izumida, Z. L. Liu: High average-power THz radiation from femtosecond laser-irradiated InAs in a magnetic field and its elliptical polarization characteristics, J. Appl. Phys. **84**, 654 (1998) 27
61. H. Ohtake, S. Ono, M. Sakai, Z. L. Liu, T. Tsukamoto, N. Sarukura: Saturation of THz-radiation power from femtosecond-laser-irradiated InAs in a high magnetic field, Appl. Phys. Lett. **76**, 1398 (2000) 27
62. C. Weiss, R. Wallenstein, R. Beigang: Magnetic-field-enhanced generation of terahertz radiation in semiconductor surfaces, Appl. Phys. Lett. **77**, 4160 (2000) 27, 28, 31
63. D. Some, A. V. Nurmikko: Coherent transient cyclotron emission from photoexcited GaAs, Phys. Rev. B **50**, 5783 (1994) 27, 28, 33, 34
64. D. Some, A. V. Nurmikko: Real-time electron-cyclotron oscillations observed by terahertz techniques in semiconductor heterostructures, Appl. Phys. Lett. **65**, 3377 (1994) 27, 28
65. R. McLaughlin, Q. Chen, A. Corchia, C. M. Ciesla, D. D. Arnone, X. C. Zhang, G. A. C. Jones, E. H. Lindfield, M. Pepper: Enhanced coherent terahertz emission from indium arsenide, J. Mod. Opt. **47**, 1847 (2000) 27, 28
66. R. McLaughlin, A. Corchia, M. B. Johnston, Q. Chen, C. M. Ciesla, D. D. Arnone, G. A. C. Jones, E. H. Linfield, A. G. Davies, M. Pepper: Enhanced coherent terahertz emission from indium arsenide in the presence of a magnetic field, Appl. Phys. Lett. **76**, 2038 (2000) 27, 28

67. J. N. Heyman, P. Neocleous, D. Hebert, P. A. Crowell, T. Muller, K. Unterrainer: Terahertz emission from GaAs and InAs in a magnetic field, Phys. Rev. B **64**, 085202 (2001) 27, 28, 29, 35, 41
68. S. R. Andrews, A. Armitage, P. G. Huggard, C. J. Shaw, G. P. Moore, R. Grey: Magnetic field dependence of terahertz emission from an optically excited GaAs p–i–n diode, Phys. Rev. B **66**, 085307 (2002) 27, 28, 29, 41, 44, 45
69. A. Corchia, R. McLaughlin, M. B. Johnston, D. M. Whittaker, D. D. Arnone, E. H. Linfield, A. G. Davies, M. Pepper: Effects of magnetic field and optical fluence on terahertz emission in gallium arsenide, Phys. Rev. B **64**, art. no. 205204 (2001) 27, 28, 35
70. D. Some, A. V. Nurmikko: Ultrafast photoexcited cyclotron emission – Contributions from real and virtual excitations, Phys. Rev. B **53**, 13295 (1996) 27, 33
71. S. Ono, T. Tsukamoto, E. Kawahata, T. Yano, H. Ohtake, N. Sarukura: Terahertz radiation from a shallow incidence-angle InAs emitter in a magnetic field irradiated with femtosecond laser pulses, Appl. Opt. **40**, 1369 (2001) 27
72. M. B. Johnston, D. M. Whittaker, A. Corchia, A. G. Davies, E. H. Linfield: Theory of magnetic-field enhancement of surface-field terahertz emission, J. Appl. Phys. **91**, 2104 (2002) 29
73. M. B. Johnston, D. M. Whittaker, A. Dowd, A. G. Davies, E. H. Linfield, X. Li, D. A. Ritchie: Generation of high-power terahertz pulses in a prism, Opt. Lett. **27**, 1935 (2002) 29, 50
74. M. B. Johnston, D. M. Whittaker, A. Corchia, A. G. Davies, E. H. Linfield: Simulation of terahertz generation at semiconductor surfaces, Phys. Rev. B **65**, 165301 (2002) 35, 41
75. A. J. Taylor, G. Rodriguez, D. Some: Ultrafast field dynamics in large-aperture photoconductors, Opt. Lett. **22**, 715 (1997) 37, 50
76. A. E. Iverson, G. M. Wysin, D. L. Smith, A. Redondo: Overshoot in the response of a photoconductor excited by subpicosecond pulses, Appl. Phys. Lett. **52**, 2148 (1988) 38, 39, 40
77. G. Rodriguez, A. J. Taylor: Screening of the bias field in terahertz generation from photoconductors, Opt. Lett. **21**, 1046 (1996) 38, 46
78. T. Dekorsy, T. Pfeifer, W. Kutt, H. Kurz: Subpicosecond carrier transport in GaAs surface-space-charge fields, Phys. Rev. B **47**, 3842 (1993) 38, 39
79. R. Kersting, J. N. Heyman, G. Strasser, K. Unterrainer: Coherent plasmons in n-doped GaAs, Phys. Rev. B **58**, 4553 (1998) 41, 42, 45, 46
80. W. Sha, A. L. Smirl, W. F. Tseng: Coherent plasma-oscillations in bulk semiconductors, Phys. Rev. Lett. **74**, 4273 (1995) 41
81. G. C. Cho, T. Dekorsy, H. J. Bakker, R. Hovel, H. Kurz: Generation and relaxation of coherent majority plasmons, Phys. Rev. Lett. **77**, 4062 (1996) 41
82. W. Fischler, P. Buchberger, R. A. Hopfel, G. Zandler: Ultrafast reflectivity changes in photoexcited GaAs Schottky diodes, Appl. Phys. Lett. **68**, 2778 (1996) 41
83. R. Kersting, K. Unterrainer, G. Strasser, H. F. Kauffmann, E. Gornik: Few-cycle THz emission from cold plasma oscillations, Phys. Rev. Lett. **79**, 3038 (1997) 41
84. C. W. Siders, J. L. W. Siders, A. J. Taylor, S. G. Park, M. R. Melloch, A. M. Weiner: Generation and characterization of terahertz pulse trains from biased, large-aperture photoconductors, Opt. Lett. **24**, 241 (1999) 46

85. A. S. Weling, T. F. Heinz: Enhancement in the spectral irradiance of photoconducting terahertz emitters by chirped-pulse mixing, J. Opt. Soc. Am. B **16**, 1455 (1999) 46, 49, 50
86. A. S. Weling, B. B. Hu, N. M. Froberg, D. H. Auston: Generation of tunable narrow-band THz radiation from large-aperture photoconducting antennas, Appl. Phys. Lett. **64**, 137 (1994) 49
87. A. S. Weling, D. H. Auston: Novel sources and detectors for coherent tunable narrow-band terahertz radiation in free space, J. Opt. Soc. Am. B **13**, 2783 (1996) 49
88. Y. Q. Liu, S. G. Park, A. M. Weiner: Terahertz waveform synthesis via optical pulse shaping, IEEE J. Sel. Top. Quantum Electron. **2**, 709 (1996) 49
89. Y. Q. Liu, S. G. Park, A. M. Weiner: Enhancement of narrow-band terahertz radiation from photoconducting antennas by optical pulse shaping, Opt. Lett. **21**, 1762 (1996) 49, 50
90. Q. Wu, X. C. Zhang: Free-space electro-optics sampling of mid-infrared pulses, Appl. Phys. Lett. **71**, 1285 (1997) 50
91. Q. Wu, X. C. Zhang: Free-space electro-optic sampling of terahertz beams, Appl. Phys. Lett. **67**, 3523 (1995) 50
92. A. Leitenstorfer, S. Hunsche, J. Shah, M. C. Nuss, W. H. Knox: Detectors and sources for ultrabroadband electro-optic sampling – Experiment and theory, Appl. Phys. Lett. **74**, 1516 (1999) 50
93. R. Huber, A. Brodschelm, F. Tauser, A. Leitenstorfer: Generation and field-resolved detection of femtosecond electromagnetic pulses tunable up to 41 THz, Appl. Phys. Lett. **76**, 3191 (2000) 50
94. H. Cao, T. F. Heinz, A. Nahata: Electro-optic detection of femtosecond electromagnetic pulses by use of poled polymers, Opt. Lett. **27**, 775 (2002) 50
95. M. C. Nuss, D. H. Auston, F. Capasso: Direct subpicosecond measurement of carrier mobility of photoexcited electrons in gallium-arsenide, Phys. Rev. Lett. **58**, 2355 (1987) 50
96. J. H. Son, T. B. Norris, J. F. Whitaker: Terahertz electromagnetic pulses as probes for transient velocity overshoot in GaAs and Si, J. Opt. Soc. Am. B **11**, 2519 (1994) 50
97. M. C. Beard, C. M. Turner, C. A. Schmuttenmaer: Measurement of electromagnetic radiation emitted during rapid intramolecular electron transfer, J. Am. Chem. Soc. **122**, 11541 (2000) 50
98. D. Cote, J. M. Fraser, M. DeCamp, P. H. Bucksbaum, H. M. van Driel: THz emission from coherently controlled photocurrents in GaAs, Appl. Phys. Lett. **75**, 3959 (1999) 50
99. A. Wetzels, A. Gurtler, L. D. Noordam, F. Robicheaux, C. Dinu, H. G. Muller, M. J. J. Vrakking, W. J. van der Zande: Rydberg state ionization by half-cycle-pulse excitation – Strong kicks create slow electrons, Phys. Rev. Lett. **89**, 273003 (2002) 50
100. C. Wesdorp, F. Robicheaux, L. D. Noordam: Displacing Rydberg electrons – The mono-cycle nature of half-cycle pulses, Phys. Rev. Lett. **87**, 083001 (2001) 50
101. C. M. Dion, A. Keller, O. Atabek: Orienting molecules using half-cycle pulses, Eur. Phys. J. D **14**, 249 (2001) 50
102. M. Machholm, N. E. Henriksen: Field-free orientation of molecules, Phys. Rev. Lett. **87**, 193001 (2001) 50

103. R. R. Jones: Creating and probing electronic wave packets using half-cycle pulses, Phys. Rev. Lett. **76**, 3927 (1996)
104. D. J. Cook, J. X. Chen, E. A. Morlino, R. M. Hochstrasser: Terahertz-field-induced second-harmonic generation measurements of liquid dynamics, Chem. Phys. Lett. **309**, 221 (1999)

Index